https://doi.org/10.5194/egusphere-2023-73
Preprint. Discussion started: 27 January 2023

Impact of the Nares Strait sea ice arches on the long-term stability of the Petermann Glacier Ice Shelf

Abhay Prakash[1,2], Qin Zhou[3], Tore Hattermann[4,5], and Nina Kirchner[1,2]

[1]Department of Physical Geography, Stockholm University, Stockholm 10691, Sweden
[2]Bolin Centre for Climate Research, Stockholm University, Stockholm 10691, Sweden
[3]Akvaplan-niva, Tromsø 9296, Norway
[4]Norwegian Polar Institute, Tromsø 9296, Norway
[5]Department of Physics and Technology, University of Tromsø, Tromsø 9019, Norway

Correspondence: Abhay Prakash (abhay.prakash@natgeo.su.se)

Abstract. One of the last remaining Greenland Ice Sheet (GrIS) glaciers featuring a floating tongue — the Petermann Glacier Ice Shelf (PGIS) is seasonally shielded by the formation of sea ice arches in the Nares Strait. However, continued decline of the Arctic sea ice extent and thickness suggest that arch formation is likely to become anomalous, necessitating an investigation into the response of PGIS to a year round mobile and thin sea ice cover. We use a high-resolution 3-D ocean-sea ice-ice shelf setup featuring an improved sub-ice shelf bathymetry and a realistic PGIS geometry, to investigate in unprecedented detail, the implications of transitions in the Nares Strait sea ice regime; from *Thick Landfast* to *Thick Mobile* and *Thin Mobile*, on the PGIS basal melt. Across all three regimes, basal melting increases occur during summer, and under the deeper (>250 m) regions of the ice shelf. Diagnosing this variability via melt rate drivers suggest that a higher thermal driving under the deeper regions causes higher melt rates, which, as a secondary effect, increases the friction velocity slightly downstream. The increased meltwater production and a stronger melt overturning in the PGIS cavity deliver more meltwater from depth to the shallower regions which lowers the thermal driving and basal melt in these regions; with the winter season showing a converse pattern. Modulations in surface forcing under a mobile and thin sea ice cover act to enhance the heat transport in the cavity, enhancing the thermal driving and friction velocity at the ice shelf base, and thereby, the basal melt. Thermodynamically, under mobile sea ice, wind upwelled Atlantic Water (AW) from the Nares Strait enter the cavity. Additionally, when sea ice thins, convective overturning drives further upwelling of AW in winter. Mechanically, wind driven inflow intensifies, and is most pronounced under a (negligibly thin) mobile summer sea ice cover; and where it acts in concert with the stronger melt overturning to enhance the friction velocity which predominantly drives the basal melt under the deeper regions. These results suggest that the projected continuation of the warming of the Arctic Ocean until the end of the 21st century and the decline in Arctic sea ice extent and thickness will amplify the basal melt, impacting the long term stability of the Petermann Glacier and its contribution to the future GrIS mass loss and sea level rise.

https://doi.org/10.5194/egusphere-2023-73
Preprint. Discussion started: 27 January 2023

1 Introduction

The Greenland Ice Sheet (GrIS) is currently the single largest contributor to sea level rise and loses mass at accelerating rates (Chen et al., 2017; The IMBIE Team, 2020; Sasgen et al., 2020). This acceleration is related to the increasing amount of heat which the warmer subsurface Atlantic Water (AW) supplies to the GrIS marine margin (Slater et al., 2019; Wood et al., 2021). Such additional oceanic heat causes enhanced basal melt and calving at marine terminating glacier fronts, which in turn leads to glacier wide dynamic thinning and flow acceleration, and disintegration of floating ice shelves with associated loss of buttressing forces on the upstream inland ice masses (Hill et al., 2018; Aschwanden et al., 2019; Rückamp et al., 2019).

Along the northern GrIS margin, the "North" and "Northeast" sectors analysed by Mouginot et al. (2019) hold an ice volume which, if melted, would cause global mean sea level to rise by 273 cm (∼37% of the total GrIS contribution). Therefore, continued presence of the few remaining buttressing ice shelves along its margin is pivotal to the sectorial and the GrIS mass balance, and its contribution to future sea level changes. However, with expected increases in basal melting driven by the ocean's response to a future warming climate, the stability of these ice shelves becomes of great concern.

Petermann Glacier (PG) has the largest discharge of all glaciers in the "North" sector, viz. 11.7 ± 1.2 Gt/yr, with a drainage basin stretching across ∼6% of the GrIS by area (Hill et al., 2017; Mouginot et al., 2019). PG terminates with a floating ice shelf, the Petermann Glacier Ice Shelf (PGIS), into the Petermann Fjord (PF). The PGIS is ∼50 km long, and its thickness ranges between ∼150 m at the calving front to ∼600 m at the grounding line (GL), where it is ∼20 km wide. With the PGIS undergoing episodic large calving events, most recently in 2010 and 2012 (Falkner et al., 2011; Münchow et al., 2014), it has been studied through various lenses. In particular, hydrographic surveys have documented the inflow of warm and saline modified AW into the PF and the PGIS cavity (Heuzé et al., 2017; Washam et al., 2018), where it drives basal melt and melt undercutting, and renders PGIS susceptible to calving. PF extends for ∼90 km before opening into the Nares Strait, which is a ∼500 km long and ∼30-50 km wide water way separating northwest Greenland from Ellesmere Island, and bridging the Lincoln Sea and Baffin Bay. Through the Nares Strait, heat and freshwater exchange between the Arctic Ocean and the western subpolar North Atlantic Ocean is facilitated (Kwok, 2005), influenced by fjord and ocean circulation and sea ice dynamics.

Sea ice covers the Nares Strait for most of the year, and observations since 1996 show that landfast winter sea ice aids the formation of ice arches which extend across the Nares Strait and thus reduce or cease ice drift through it. Typically, a northern ice arch forms near the Lincoln Sea entrance to the Nares Strait and/or a southern one near the Smith Sound/Kane Basin region, with interannual variability in exact location and duration, and associated variations in sea ice transport through the Nares Strait (Kwok, 2005; Kwok et al., 2010; Münchow, 2016; Ryan and Münchow, 2017; Moore et al., 2021). During summer, sea ice is mobile for a short period of time. For a seasonal cycle of winter landfast sea ice and summer mobile sea ice, modelling of ice shelf-ocean interactions at the PGIS demonstrated that changes in ocean circulation induced by changes in sea ice mobility and the resulting upwelling of AW increased the modelled PGIS basal melt rates by 20% (Shroyer et al., 2017).

In 2007, neither of the ice arches formed. Sea ice area and volume outflow through a flux gate across the Robeson Channel were reported to be not only the highest, but also more than twice the annual mean over the years 1997-2009 (Kwok et al., 2010). In 2019, when both the ice arches again failed to form, ice area flux through the Robeson Channel flux gate exceeded

https://doi.org/10.5194/egusphere-2023-73
Preprint. Discussion started: 27 January 2023

the one reported from 2007. Yet, ice volume flux was less, due to reduced sea ice thickness (Moore et al., 2021). The 2019 event was preceded by a collapse of the northern ice arch in May 2017 and its complete absence in 2018, during which the southern arch persisted only for a short period (Moore and McNeil, 2018; Moore et al., 2021). Notably, between 1997 and 2019, the time period during which ice arches were present in the Nares Strait reduced by 7 day/year (Moore et al., 2021).

A continued decline in the Arctic sea ice thickness (Maslanik et al., 2011; Kwok, 2018; Kacimi and Kwok, 2022) and ice arch formation duration, and the resulting increased outflow of the thick Arctic multiyear ice further expedites the transition towards a thin (and mobile) sea ice cover and makes ice arch formation more unlikely. The loss of ice arches implies that the seasonal cycle of sea ice mobility in the Nares Strait ceases and that instead, year round mobile sea ice conditions start to prevail (Moore et al., 2021). Moreover, such a scenario is expected to continue in the future as the Arctic sea ice continues to decline in extent and thickness, and the Arctic Ocean is projected to be sea ice free during at least one summer before 2050 CE (Wang and Overland, 2012; Meredith et al., 2019; Pörtner et al., 2019; Notz and SIMIP Community, 2020). Consequences that these changes may have on the oceanic heat transport (e.g. via air-sea thermal and haline buoyancy fluxes and momentum transfer) toward the PGIS cavity, with ramifications for the long term stability of the PGIS, remain largely unknown.

Here, implications of changes in the Nares Strait sea ice regime - from a landfast, thick sea ice cover to a mobile, thin one - on the PGIS basal melt are investigated. A high-resolution unstructured grid 3-D ocean-sea ice-ice shelf setup is used to capture the circulation in the wider Nares Strait region, and which utilizes an improved sub-ice shelf bathymetry and a realistic ice shelf geometry to resolve the circulation in the PF and the PGIS cavity in unprecedented detail (see Prakash et al., 2022).

2 Methods

2.1 Model setup

The unstructured grid, free-surface, 3-D primitive equation Finite Volume Community Ocean Model (FVCOM) (Chen et al., 2007) has recently been amended by an ice shelf module (Zhou and Hattermann, 2020) that allows modelling of oceanic processes in ice shelf cavities bounded by complex coastal geometries and fjord bathymetry. Further, a new sea ice module (*Ice Nudge*) was implemented (Prakash et al., 2022) that allows to prescribe sea ice concentration (A_i), sea ice thickness (h_i), sea ice salinity (S_i) and sea ice velocities ($\boldsymbol{U}_\mathrm{i}$) as external surface boundary conditions to modulate the air-sea exchanges of buoyancy and momentum, and ocean dynamics. The model has further been adapted to render a nested high resolution 3-D ocean-sea ice-ice shelf setup for the PGIS and PF. For a detailed description of the model setup and a standard run (including selected results from it), see Prakash et al. (2022).

The modelling domain stretches from 75° to 87° N and 29° to 81° W, covering the PF and Nares Strait with open boundaries located in the Lincoln Sea and Baffin Bay (Figure 1(a)). Figure 1(b) indicates the cross-section locations in the PF and adjacent Hall Basin and Nares Strait regions at which modelled results are presented in later sections. The horizontal grid is composed of non-overlapping unstructured triangular cells with variable resolution: 200 m in the fjord, 2 km in the near-fjord regions and 4 km elsewhere. The vertical grid comprises of 23 terrain-following σ-layers. The fjord bottom topography and the PGIS draft have been derived from BedMachine v3 (Morlighem et al., 2017), wherein the latter represents a period prior to the 2010

https://doi.org/10.5194/egusphere-2023-73
Preprint. Discussion started: 27 January 2023

calving event. As described in Prakash et al. (2022), the BedMachine v3 dataset has been modified to remedy an inaccurately represented sub ice shelf water column thickness along the coastline and underneath the thickest regions of the PGIS, and to include a ∼ 540-610 m deep inner sill located ∼ 25 km from the GL (Tinto et al., 2015) which is not included in the dataset.

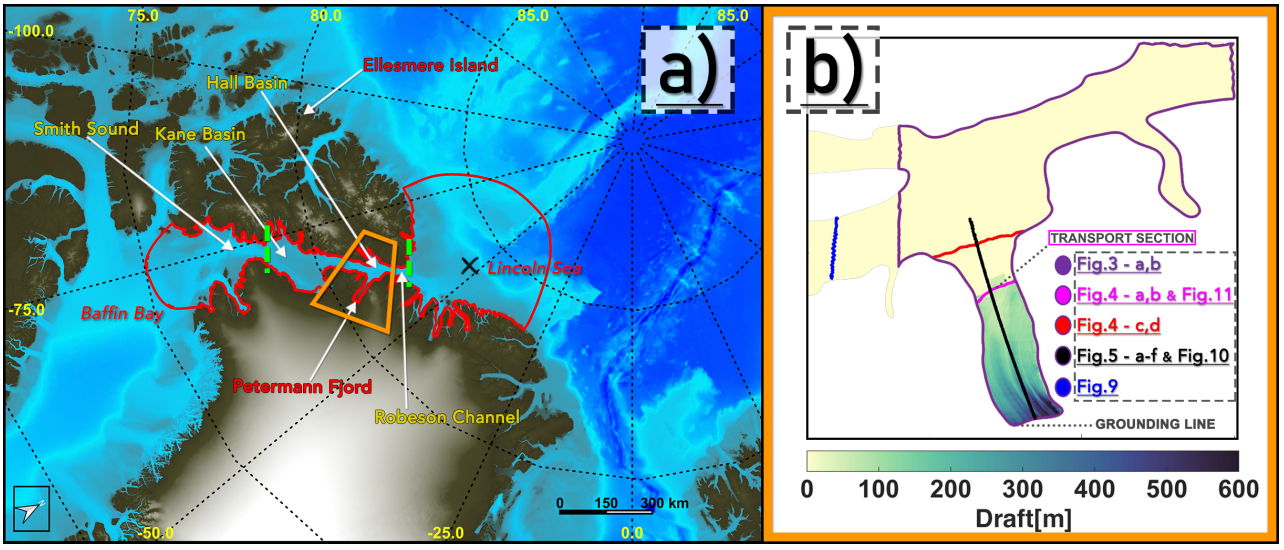

Figure 1. (a) Overview map, modified from the IBCAO V4 Grid (Jakobsson et al., 2020a) with longitude and latitude expressed in °East and °North, respectively. The FVCOM model domain is outlined in red, with lateral boundaries defined by the Greenland and Ellesmere Island coastlines, and open ocean boundaries in the Lincoln Sea and Baffin Bay. The northern sill region in the Lincoln Sea is highlighted by a black 'X' symbol. Yellow-labelled white arrows point to regions of interest within Nares Strait. Dashed green lines mark the approximate locations where the northern (near Robeson Channel) and southern (between Kane Basin and Smith Sound) sea ice arches usually form. The orange box indicates a smaller PF, Hall Basin and Nares Strait region within which model results are presented. (b) Zoom into the orange box in panel (a). Modelled ice shelf draft (in meters) of the Petermann Glacier in PF. Lines show locations of cross-sections for which model results are presented in subsequent figures according to color-coded legend. Note that the transport section is the same as in Figure 4(a,b).

2.2 Experiment setup

To study the implications of a possible regime shift in sea ice arch formation in the Nares Strait for the PGIS basal melt, three experiments, differing in sea ice concentration, thickness and mobility, which are imposed through the *Ice Nudge* module (Prakash et al., 2022), are conducted. These are the *1. Thick Landfast*, *2. Thick Mobile*, and *3. Thin Mobile* experiments. The *Thin Mobile* run features a thin and year round mobile sea ice, facilitated by the absence of ice arches, and mirroring an increasingly often observed (and likely standard future) scenario (see further below), cf. Table 1, Figure 2. Note that the *Thin Mobile* run is identical to the *Standard run* introduced in Prakash et al. (2022), while the *Thick Landfast* and *Thick Mobile* experiments are constructed as perturbations to the *Thin Mobile* run.

https://doi.org/10.5194/egusphere-2023-73
Preprint. Discussion started: 27 January 2023

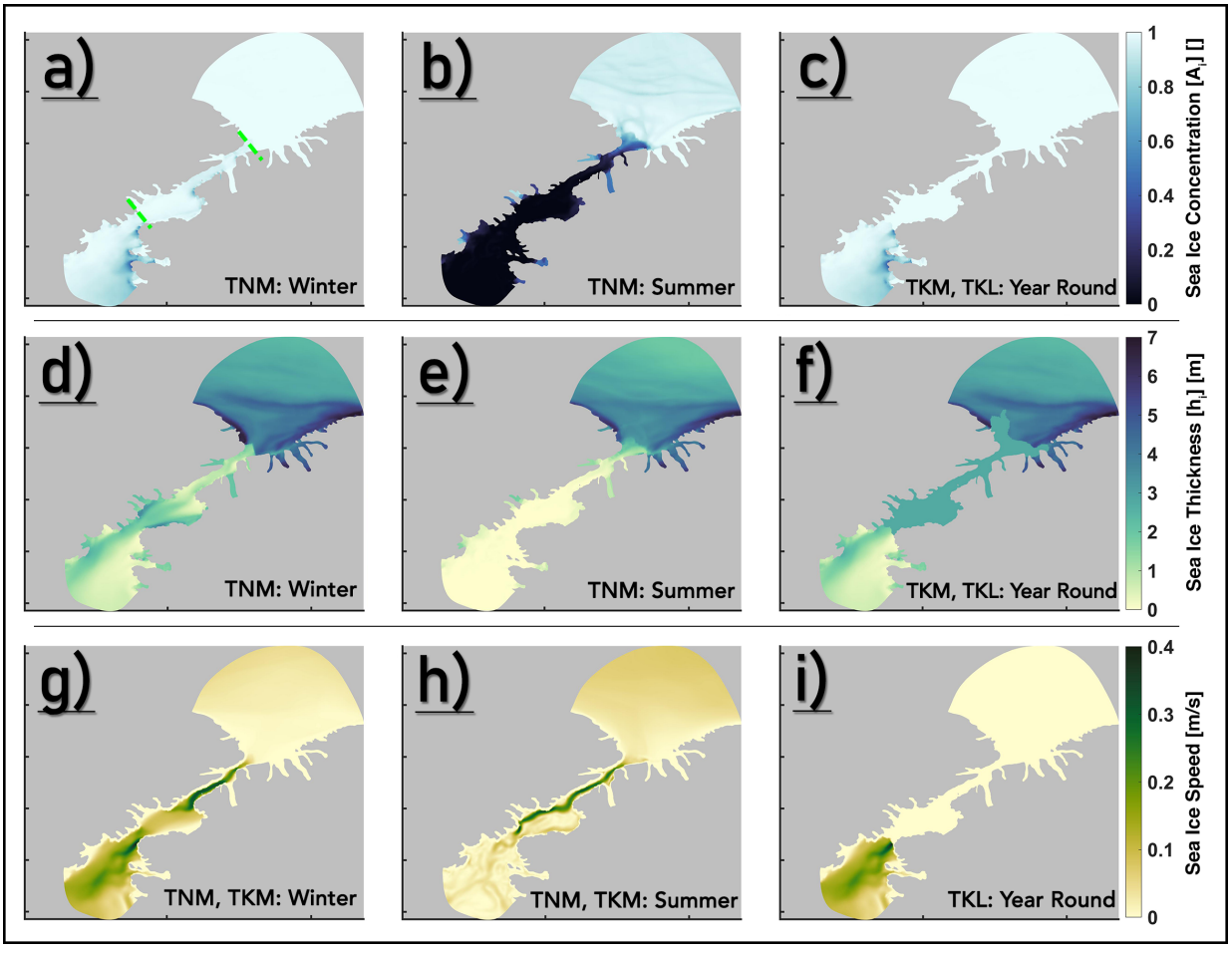

Figure 2. Winter (left column; panels a, d, g), summer (middle column; panels b, e, h) and year round (right column; panels c, f, i) sea ice forcing for the *Thin Mobile* (TNM), *Thick Mobile* (TKM), and *Thick Landfast* (TKL) experiments. Speed, in panels g-i, is the magnitude of the velocity. Approximate locations of the northern and southern arch are indicated as dashed green lines in panel a. Note that the TKL sea ice speed (panel i) is designed to create year round landfast (zero speed) sea ice conditions until the southern arch. South of it, sea ice speeds are similar to TNM, TKM, and as an example, winter speeds south of the southern arch are shown in panel (i).

The *Thick Mobile* experiment, with a thick and mobile sea ice cover, such as after a premature collapse of an ice arch (as e.g. observed in 2017, (Moore and McNeil, 2018)), represents an intermediate regime between the *Thick Landfast* (see below) and the *Thin Mobile* runs. In the *Thick Mobile* experiment, A_i = 1 is chosen to ensure that the region bounded by the sea ice arches (see Figure 2, Table 1) is completely ice covered, which affects seasonality via removal of open ocean during summer. Additionally, h_i = 2.75 m ensures that the ice cover is sufficiently thick so as to block the heat exchange between the ocean and the local atmosphere. Lastly, the (nonzero) sea ice velocities are retained from the *Thin Mobile* run. The *Thick Landfast* experiment with thick, landfast sea ice mimics conditions prevailing in the late 1990's - early 2000's when ice arches regularly blocked the southward sea ice flux for large parts of the year (Kwok et al., 2010). Ice flux stoppage estimates from Kwok et al.

https://doi.org/10.5194/egusphere-2023-73
Preprint. Discussion started: 27 January 2023

(2010) during these years suggest a landfast sea ice cover over the model winter and summer periods. In the *Thick Landfast* experiment, sea ice conditions in the *Thick Mobile* experiment are perturbed further by setting the sea ice velocities in the *Thick Mobile* experiment in the region bounded by the sea ice arches to zero, which additionally blocks the transfer of momentum onto the ocean (Figure 2, Table 1). The chosen h_i in the *Thick Mobile* and *Thick Landfast* experiments is well within the range of sea ice draft values reported in this region (Ryan and Münchow, 2017), and corresponds to the presence of the old Arctic multiyear ice that are likely advected from the north (of the northern arch) into the Nares Strait, and which are either fastened in place under a landfast regime, or are advected southward following the collapse of the ice arches.

	Thick Landfast (TKL)	Thick Mobile (TKM)	Thin Mobile (TNM)
Runtime start (dd-mm-yyyy)	01-01-2016*	01-01-2016*	01-01-2016
Runtime end (dd-mm-yyyy)	01-01-2017	01-01-2017	01-01-2017
Sea ice dynamics	**landfast**	mobile	mobile
Winter mean sea ice cover A_i [-]	**1**	**1**	∼0.96
Winter mean sea ice thickness h_i [m]	**2.75**	**2.75**	∼0.89
Summer mean sea ice cover A_i [-]	**1**	**1**	∼0.12
Summer mean sea ice thickness h_i [m]	**2.75**	**2.75**	∼0.34

Table 1. Numerical experiment characteristics.The winter and summer seasons correspond to days 30-105 and 170-245 of the 2016 calendar year. *The *Thick Landfast* and *Thick Mobile* experiments are initialised using the *Thin Mobile (i.e. Standard run)* run solution on January 01, 2016 00:00:00 UTC with perturbed sea ice conditions. Perturbations in the sea ice conditions in the *Thick Landfast* and *Thick Mobile* experiments with respect to the *Thin Mobile* run are highlighted in bold. A mobile sea ice cover utilises sea ice velocity solutions from the A4 ROMS-CICE run. For a landfast sea ice cover, those are set to zero in the region bounded by the sea ice arches. The sea ice characteristics described above represent the mean conditions in the Nares Strait region bounded by the northern and southern sea ice arches (Figure 2(a)).

Model results are presented for the year January 01, 2016 00:00:00 UTC - January 01, 2017 00:00:00 UTC, as it is closest to the (2016-2019) period, which has been characterised by frequent collapse/absence of ice arches, reduced ice flux stoppages and extraordinarily high ice area flux through the Nares Strait (Moore et al., 2021), for which the model can be be initialised and run using realistic atmosphere, ocean and sea ice boundary conditions. Note that the simulation period spans from July 01, 2014 00:00:00 UTC - January 01, 2017 00:00:00 UTC. The surface forcing for the atmospheric and sea ice conditions for this period are obtained from the polar (p) version of the RACMO2.3p2 (Regional Atmospheric Climate Model, Noël et al., 2019) and the coupled A4 ROMS (4-km pan-Arctic Regional Ocean Modeling System grid) - CICE (Community Ice CodE) run (Hattermann et al., 2016; Hunke et al., 2010) respectively. Therein, the state of sea ice, and the mechanical and thermal fluxes to the ocean at the sea ice-ocean interface are imposed as a surface boundary condition to the model using the *Ice Nudge* module (cf. Prakash et al. (2022)). The A4 ROMS-CICE run forms the northern sea ice arch, with thick (multiyear) fast ice conditions north of it, and a thin, year round mobile ice to its south (Figure 2(a,b,d,e,g,h)). A younger, thinner and mobile modelled sea ice cover in the Nares Strait agrees well with the findings reported by Moore et al. (2021) and Kacimi and Kwok

https://doi.org/10.5194/egusphere-2023-73
Preprint. Discussion started: 27 January 2023

(2022). Therefore, the *Standard run* sea ice cover introduced in Prakash et al. (2022) is representative of a present-day thin, mobile sea ice cover and is thus here called the *Thin Mobile* run. As described in Prakash et al. (2022), the FVCOM grid is nested within the A4 ROMS grid. This, in conjunction with the 5 km AOTIM (Arctic Ocean Tidal Inverse Model, Padman and Erofeeva, 2004), is used to provide hourly ocean boundary conditions. Bias-corrected monthly climatologies of temperature, salinity and velocity fields are constructed for the simulation period using the 2007-09 average of the corresponding fields from the A4 hindcast, which are interpolated to hourly forcing intervals. Further, the hourly AOTIM sea surface height (SSH) solution from the simulation period is added to the A4 SSH field from the same period to generate the tidal forcing (see Prakash et al., 2022 for details).

2.3 Model output and diagnostics

The primitive equations are solved in the spherical coordinate system, and the daily averaged seawater potential temperature (θ), salinity (S), east- and northward velocity (u, v), and the ice shelf basal melt rates used in this study are available as direct FVCOM model outputs. The u (eastward) and v (northward) velocity components from the model are transformed into Cartesian u_x (X-axis) and v_y (Y-axis) components when calculating the transport diagnostics (see below). Moreover, the *Ice Nudge* module provides several prognostic variables related to ocean and sea ice-ocean (thermo)dynamics (see Prakash et al., 2022 for details). For instance, brine released during sea ice formation is captured in the variable *Virtual Salt Flux* (F_S), provided in kg m^{-2} s^{-1} and converted to mm/day, and the variable *Salinity of the uppermost layer* (S_w), is provided in psu.

Calculating the overturning streamfunction (Ψ) and the overturning heat transport (Φ) normal to a cross-section in an unstructured grid representation of the PF area requires accounting for a non-uniform lateral and vertical cross-sectional geometry. Firstly, the u, v and θ fields are needed at each cell index along the transect (Figure 1(b)) across which the calculations are made. Note that the θ field stored on the FVCOM nodes are interpolated to the cell centers. Then, the angle α between the X-axis and the true eastward direction is computed and u and v are transformed into u_x and v_y (cf. Sect. 3.1.), viz.

$$u_x(i,j,\tau) = u(i,j,\tau)\cdot\cos\alpha + v(i,j,\tau)\cdot\sin\alpha; \quad v_y(i,j,\tau) = -u(i,j,\tau)\cdot\sin\alpha + v(i,j,\tau)\cdot\cos\alpha \tag{1}$$

where $i = 1,\ldots,n$ represents the transect cell index, $j = 1,\ldots,m$ the σ-layer, and $\tau = 1,\ldots,366$ an index referencing the daily averaged model output intervals.

To integrate the transport normal to the transect, the flux is discretized laterally across the $k = 1,...,n-1$ edge segments that are bounded by two successive cell indices, i and $i+1$. In the vertical, along the transect, the depth coordinates associated with the FVCOM nodes are interpolated to the cell centers. At each transect cell index, the difference between the successive sigma level depths at the cell centers gives the thickness of each of the 23 terrain following σ-layers. The angle ϕ between the X-axis and the edge segment bounded by any two successive cell indices i, $i+1$, at all corresponding vertical levels j, with coordinates ($x_c(i,j)$,$y_c(i,j)$) and ($x_c(i+1,j)$, $y_c(i+1,j)$), respectively, is computed as

$$\phi(k,j) = \text{atan2}\left(y_c\,(i+1,j) - y_c(i,j),\, x_c(i+1,j) - x_c(i,j)\right). \tag{2}$$

https://doi.org/10.5194/egusphere-2023-73
Preprint. Discussion started: 27 January 2023

These angles are then used to compute the normal flow ($u_\perp$) corresponding to each output interval τ and vertical level j at the two i, $i+1$ cell indices abbreviated in the following by $\diamond$ as

$$u_\perp(\diamond,j,\tau) = u_x(\diamond,j,\tau)\cdot\sin\phi(k,j) - v_y(\diamond,j,\tau)\cdot\cos\phi(k,j)\,. \tag{3}$$

The vertically integrated normal flow Ψ_z at each output interval τ is then computed as

$$\Psi_z(\diamond,\tau) = \int_{surf}^{H} u_\perp(\diamond,j,\tau)\cdot dz(\diamond,j)\,, \tag{4}$$

where $surf$ is the ocean surface, or the base of the PGIS draft for sub ice shelf transects, and H is the depth of the seafloor, at cell indices i and $i+1$. $dz(\diamond,j)$ represents the thickness of the corresponding σ-layer j.

For each τ, the associated vertically integrated normal temperature flow Φ_z is calculated as

$$\Phi_z(\diamond,\tau) = \int_{surf}^{H} \rho\cdot c_p\cdot(\theta(\diamond,j,\tau)-\theta_f)\cdot u_\perp(\diamond,j,\tau)\cdot dz(\diamond,j)\,, \tag{5}$$

where ρ = 1026 kg m^{-3} is the density of seawater, c_p = 3.97 kJ kg^{-1} °C^{-1} is its specific heat capacity, and θ_f = -2.4 °C is the freezing point of seawater at the GL depth. Note that $u_\perp\cdot dz$ and $\rho\cdot c_p\cdot(\theta-\theta_f)\cdot u_\perp\cdot dz$ for any cell index i and vertical level j represents the (heat) transport through the σ-layer j at cell index i.

Then, for each τ, the vertically integrated mean flow $\overline{\Psi}_z$, and the associated vertically integrated mean temperature flow $\overline{\Phi}_z$ normal to the discretized edge segment k bounded by cells i and $i+1$ is computed as

$$\overline{\Psi}_z(k,\tau) = \frac{|\Psi_z(i,\tau)|+|\Psi_z(i+1,\tau)|}{2}; \qquad \overline{\Phi}_z(k,\tau) = \frac{|\Phi_z(i,\tau)|+|\Phi_z(i+1,\tau)|}{2}\,. \tag{6}$$

Thickness ($dr(k)$, in meters) of the discretized flow sections bounded by cells i and $i+1$ is calculated as

$$dr(k) = \sqrt{(x_c(i+1)-x_c(i))^2+(y_c(i+1)-y_c(i))^2}\,. \tag{7}$$

Laterally integrating the vertically integrated mean normal (heat) transport $\overline{\Psi}_z(k,\tau)\cdot dr(k)$ and $\overline{\Phi}_z(k,\tau)\cdot dr(k)$, through the small edge segments k of thickness dr, gives the overturning streamfunction Ψ (in m^3 s^{-1}) and the associated overturning heat transport Φ (in kJs^{-1}, converted to Watts (W)), at each output interval τ, normal to the transect,

$$\Psi(\tau) = \int_{x_w}^{x_e} \overline{\Psi}_z(k,\tau)\cdot dr(k); \qquad \Phi(\tau) = \int_{x_w}^{x_e} \overline{\Phi}_z(k,\tau)\cdot dr(k), \tag{8}$$

https://doi.org/10.5194/egusphere-2023-73
Preprint. Discussion started: 27 January 2023

where, x_w and x_e, respectively, are the western and eastern PF boundaries at the transect.

Further, evaluating Equation 6, 7, and 8 only for the positive/negative values, or for both the positive and negative values of $\Psi_z(\diamond,\tau)$ and $\Phi_z(\diamond,\tau)$, respectively, yields the mean inflow/outflow or the net flow in $m^3\ s^{-1}$, and the associated heat inflow (H_{IN})/outflow (H_{OUT}) or the net heat flow (H_{NET}) in kJs^{-1}, converted to Watts (W).

3 Results

Below, the seasonal mean ocean circulation and ice shelf basal melt rates at the PGIS are described first for the *Thick Landfast* run. Here, the drivers of PGIS basal melt, viz., an energetic circulation and strong thermal forcing in the cavity are analysed (Sect. 3.1.1, 3.1.2) and their contribution to the basal melt are presented in Sect. 3.1.3. Then, these results are compared to the *Thick Mobile* and *Thin Mobile* scenarios, in order to discern the seasonal thermo-mechanical contributions of sea ice extent, thickness and mobility to the ocean circulation and their impact on the PGIS basal melt (Sect. 3.2.1, 3.2.2, and 3.2.3).

3.1 Thick Landfast run

3.1.1 Depth averaged seasonal mean currents in the PF and the PGIS cavity

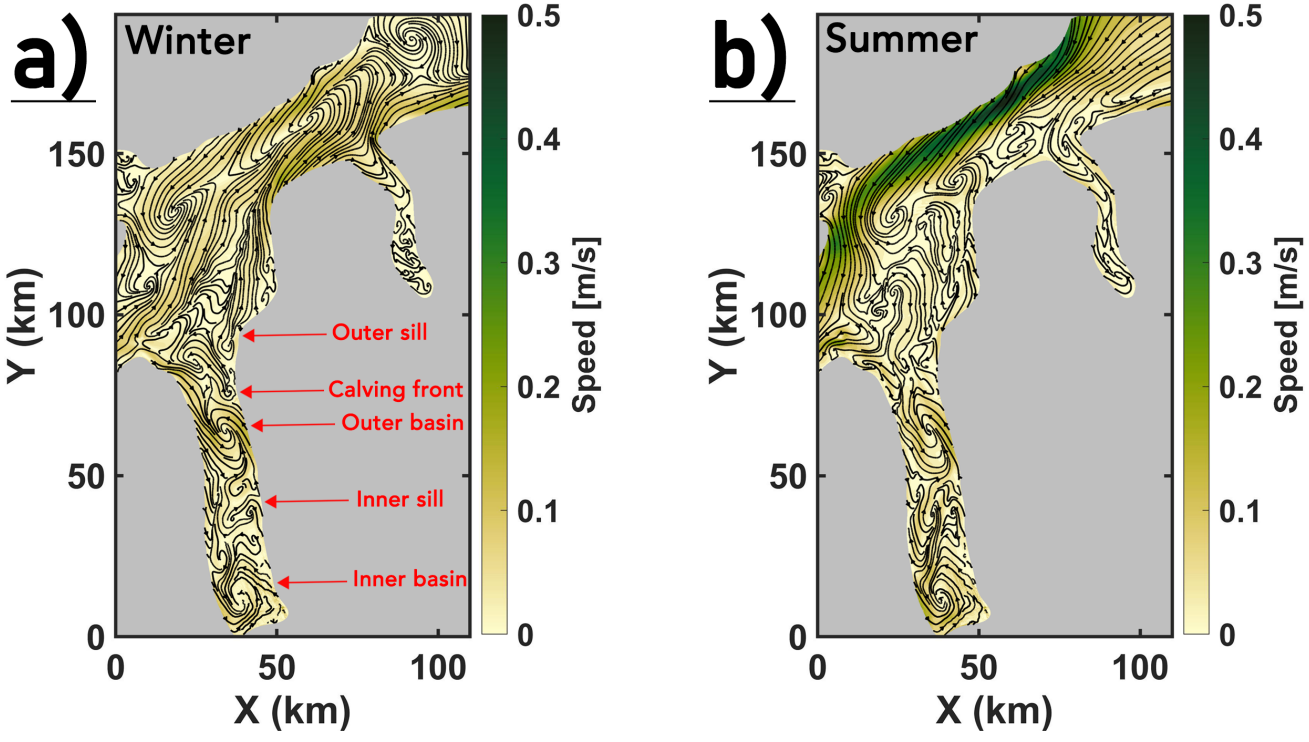

Figure 3. Depth averaged seasonal mean speed for (a) winter and (b) summer with the mean streamlines overlaid for the area indicated in Figure 1(b). Selected topographic features in PF are labelled (in red) in panel (a).

https://doi.org/10.5194/egusphere-2023-73
Preprint. Discussion started: 27 January 2023

The depth- and seasonally (Table 1) averaged circulation in the wider PF area is shown in Figure 3(a,b). In summer, a general southward current is observed in the Nares Strait which has a cross-strait component in the Hall Basin region, however, the circulation in winter appears more complex because of several flow reversals in the Robeson Channel and the Hall Basin region. Mean speeds during winter are generally lower than summer, when speeds attain their highest values along the Canadian Nares Strait coast. Near the mouth of PF, irrespective of the season, the circulation is characterized by lateral inflow and outflow supported by the western and eastern coastal boundaries, respectively (as modelled by Shroyer et al., 2017, see Sect. 4.1.1). Moreover, a cyclonic (counter-clockwise) gyre enables exchange between the PF and Hall Basin (as observed by Johnson et al., 2011, see Sect. 4.1.1). Underneath the thickest regions of the ice shelf draft, close to the GL, a similar cyclonic circulation pattern is formed, seaward of which, an anticyclonic flow resides over the inner-sill region.

3.1.2 Seasonal mean normal flow across the outer sill and into the PGIS cavity

Across the mouth of the PF and the PGIS (cf. Figure 1(b)) the seasonal mean flow normal to them are shown in Figure 4. Specifically, winter season conditions in the PGIS cavity (Figure 4(a)) and at the mouth of PF (Figure 4(c)) are displayed, as are corresponding summer season conditions (Figure 4(b,d)). Mean isotherms and isopycnals are overlaid on all panels.

In the PGIS cavity, irrespective of the season, inflow (positive normal velocities) and outflow (negative normal velocities) are largely confined to the western and eastern regions of the fjord, respectively (Figure 4(a,b)). In winter (Figure 4(a)), inflow (outflow) of up to ∼0.15 m/s (∼-0.15 m/s) directed into (out of) the PGIS cavity is modelled. At the GL depth of ∼600 m, water masses are characterized by a potential temperature $\theta \sim$ -0.8°C, and a potential density anomaly (referenced to 0 dbar) σ_0 ∼27.3 kg/m^3. Near-bottom temperature, at depths of ∼ 1100 m, is $\theta_{\text{bottom}} \sim$ -0.6°C. In summer (Figure 4(b)), outflow is stronger than winter, and inflow intensifies in the western fjord sector at depths of ∼600-1050 m where velocities reach ∼0.35 m/s. Further, the water masses are warmer and saltier in summer compared to winter, with modelled $\theta \sim$ -0.5°C and σ_0 ∼27.5 kg/m^3 at the GL depth, and $\theta_{\text{bottom}} \sim$ -0.4°C, indicating a larger admixture of AW into the cavity during that season (discussed further in Sect. 4.1.2).

Near the fjord mouth (Figure 4(c,d)), mean velocity attains magnitudes of about 0.1 m/s. While a similar distribution of inflow (west) and outflow (east) is largely retained here in winter (Figure 4(c)), in summer, a strong subsidiary outflow (Figure 4(d)) is seen in the ∼50-250 m depth range close to the western flank (as observed by Heuzé et al. (2017); see discussions in Sect. 4.1.2). In winter, water masses with σ_0 ∼27.4 kg/m^3 and $\theta_{\text{bottom}} \sim$ -0.6°C occupy the greater depths (∼500 m) seaward of the outer sill, whereas, in summer, those are denser (σ_0 ∼27.5 kg/m^3) and show a ∼50% increase in the near-bottom temperatures.

With the transport diagnostics described in Sect. 2.3, a winter (summer) mean glacierward heat inflow (H_{IN}) of ∼2.6 (∼3.3) TW, or ∼12% (∼13%) lower (higher) than the annual mean heat inflow of ∼2.92 TW is computed normal to the PGIS cross-section (Figure 1(b)). The corresponding mean winter (summer) outflow is ∼ -2.39 (∼ -2.81) TW. Thus, a net mean winter (summer) heat flow of ∼0.21 (∼0.49) TW, or ∼62% (∼44%) lower (higher) than the net mean annual heat flow of ∼0.34 TW, is directed into the PGIS cavity (see Sect. 4.1.3; further discussed in the context of changing sea ice cover in 3.2.3 and 4.2.3).

https://doi.org/10.5194/egusphere-2023-73
Preprint. Discussion started: 27 January 2023

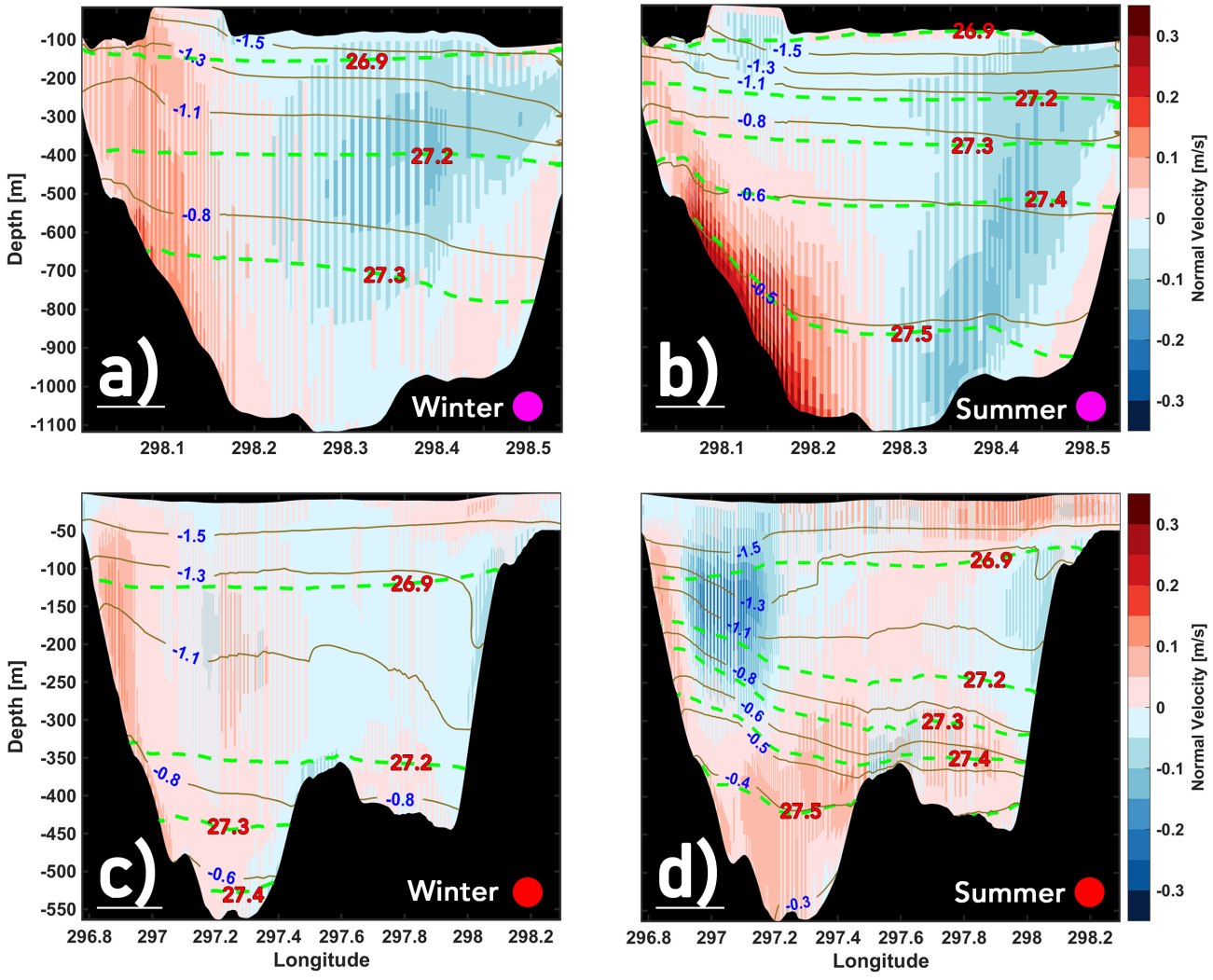

Figure 4. Seasonal mean normal velocity with mean isotherms (brown solid line, blue label) and mean isopycnals (green stippled line, red label) for PGIS winter (a), summer (b), and PF mouth winter (c) and summer (d) conditions. For locations of cross-sections, see Figure 1(b).

3.1.3 Oceanic controls on the PGIS basal melt for the Thick Landfast run

225 The modelled annual mean, and the winter and summer mean anomalies relative to it are shown for the temperature and salinity profiles (Figure 5(a-f); transect stretching from the fjord mouth (left margin) to the GL (right margin)), and the PGIS basal melt rates (Figure 6 (a-c)). Further, the winter and summer mean anomalies (with respect to the annual mean) of the drivers of melt, viz., the thermal driving (ΔT) and the friction velocity (u^*) that regulates the shear driven turbulent heat transfer across the ice-ocean boundary (see Zhou and Hattermann (2020) for details) are shown (Figure 6(d-i)).

https://doi.org/10.5194/egusphere-2023-73
Preprint. Discussion started: 27 January 2023

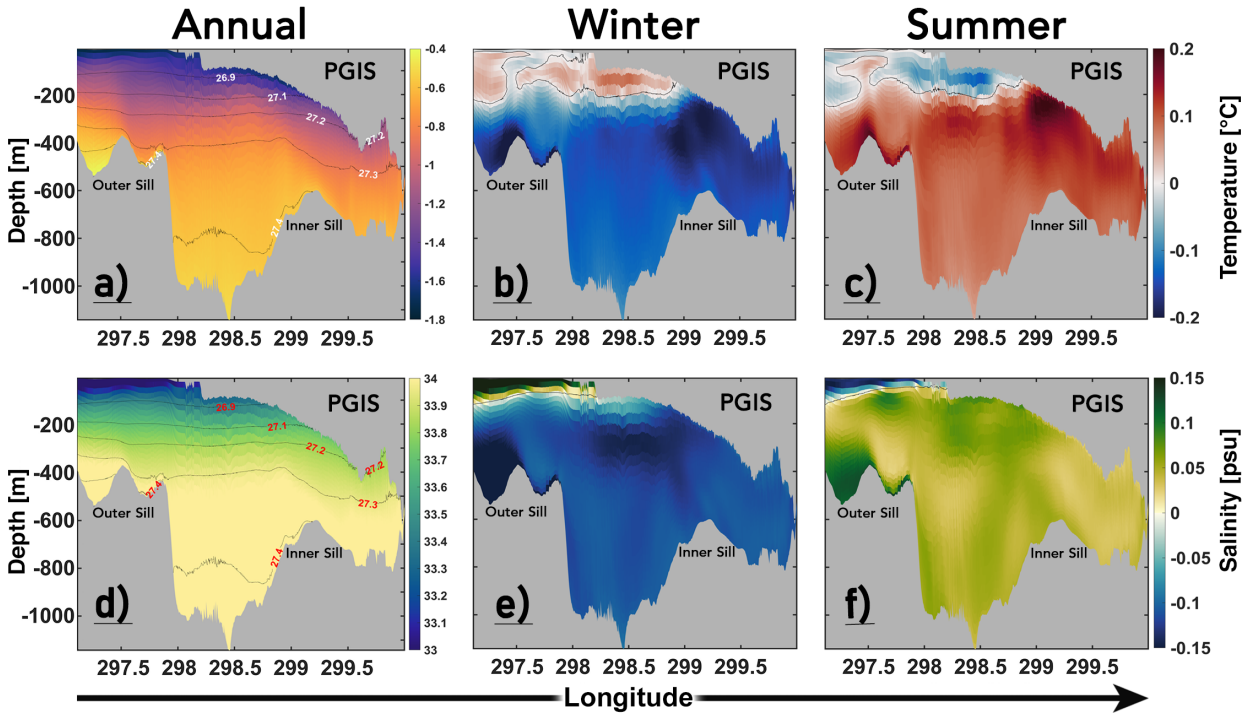

Figure 5. Annual mean temperature (a) and salinity (d) along the PF; see Figure 1(b) for the cross section location. Winter and summer temperature (b,c), and salinity (e,f), anomalies are shown relative to the annual mean. Since anomalies are plotted, the range and scale of temperature and salinity (scalebars given in panels c and f) are different from those used to plot the annual means (panels a and d).

The annual mean temperature and salinity of the water masses that overflow the inner sill and reach the GL are ∼-0.7°C and ∼34 psu (σ_0=27.3 kg/m^3) (Figure 5(a,d)). Compared to the annual mean, at the GL depth, during winter (summer), waters entering the inner fjord basin are up to ∼0.18°C colder (∼0.12°C warmer), and up to ∼0.12 psu fresher (∼0.05 psu saltier), with strongest losses (gains) seen over the inner sill (Figure 5(b,c,e,f)). However, there are also regions under the shallower outer regions of the PGIS and the PF mouth with negligible temperature gain (loss) in winter (summer) of up to ∼0.1°C. The presence of a warmer (summer) AW near the seafloor over the outer sill and under the deeper regions of the PGIS base (Figure 5(c)), and an energetic summer circulation (Figure 3, 4), imply increased basal melt rates (Figure 6(a-c)). A colder anomaly beneath the shallower ice base during summer (Figure 5(c)) indicates a more vigorous outflow of glacial meltwater (see Figure 4 and discussion in Sect. 4.1.2), which lowers the basal melt rate in the central and western sector of the PGIS (Figure 6(a-c)).

The annual mean melt rates show strong spatial variability, largely ranging from a few m/yr to ∼100 m/yr (Figure 6(a)). The winter (summer) mean melt rate anomalies reflect the seasonal changes in ocean properties; being predominantly lower (higher) compared to the annual mean values, and with regions along the western fjord sector near the PGIS calving front showing nominal gains (losses) of up to ∼5 m/yr (Figure 6(b,c)). The annual mean melt rate averaged over the entire PGIS base is calculated as ∼24.1 m/yr, with winter (summer) mean modelled melt rates being ∼17.9 m/yr (∼30.3 m/yr), or ∼26% lower (higher) than the annual mean. The annual mean basal melt (and its winter and summer anomalies) strengthens seaward

https://doi.org/10.5194/egusphere-2023-73
Preprint. Discussion started: 27 January 2023

of the GL, with peaks seen slightly north of the GL, and decreases thereafter (Figure 6(a-c)). Furthermore, there are regions of strong melt (and melt anomalies) aligned with the PGIS flow direction (Figure 6(a-c)), with winter (summer) mean modelled basal melt rate anomalies exceeding (subceeding) the mean annual basal melt rates; and by up to ∼50 m/yr on the eastern sector (Figure 6(b,c)). Also, substantial lateral variability is observed in the annual mean melt rate (and melt rate anomaly) signals. The mean modelled magnitude and spatial characteristics of the PGIS basal melt compare well with estimates reported in Wilson et al. (2017), Rignot and Steffen (2008), Washam et al. (2018) and are further discussed in Sect. 4.1.3.

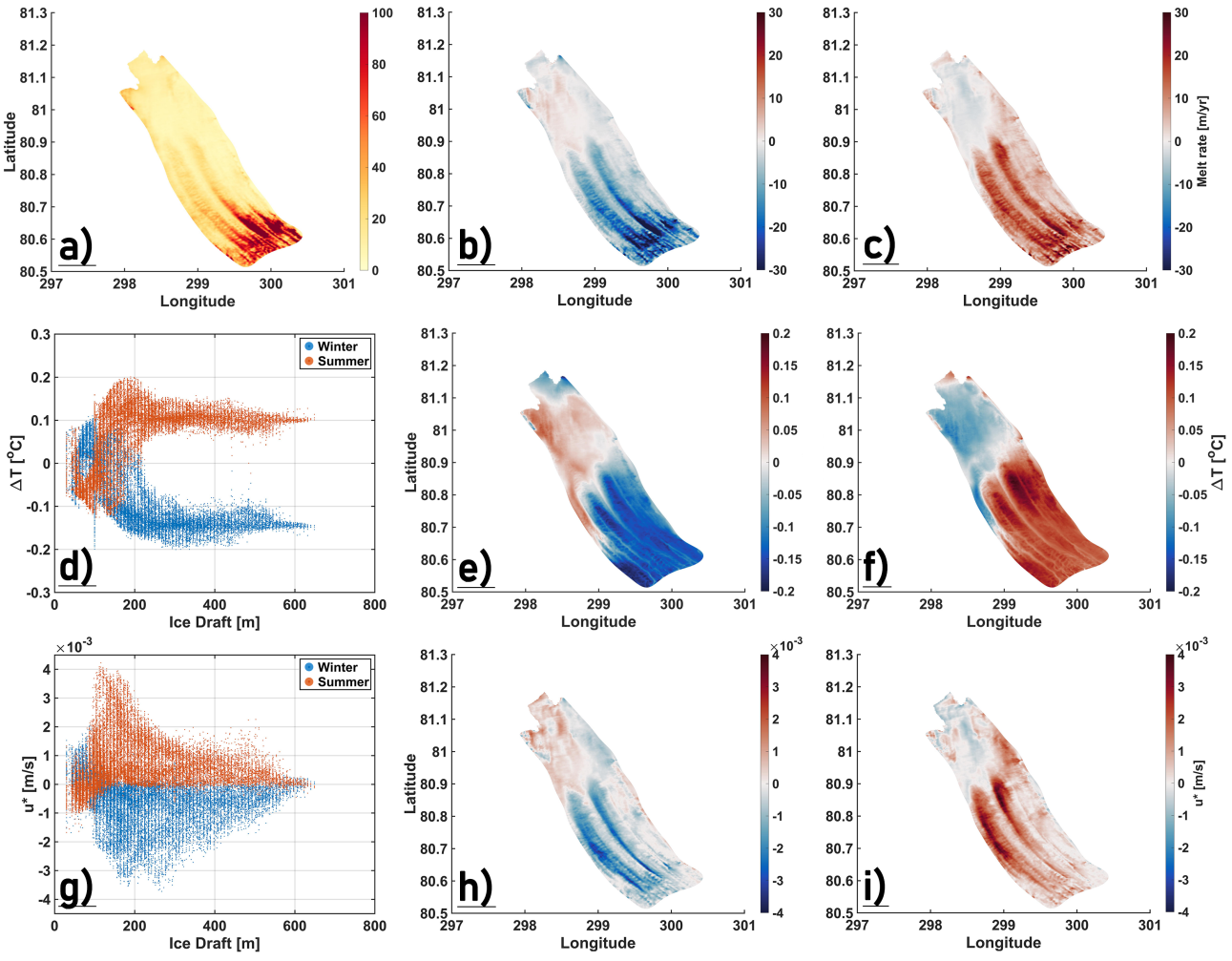

Figure 6. PGIS annual (2016) mean modelled melt rate (a), and winter (b) and summer (c) mean anomalies relative to it for the *Thick Landfast* run. Winter and summer mean anomalies of the thermal driving (ΔT) (d-f) and the friction velocity (u^*) (g-i) relative to the corresponding annual mean at the PGIS base for the *Thick Landfast* run; plotted vs. ice draft (d,g) and as winter (e,h) and summer (f,i) anomaly maps.

In summer, there is an increase in ΔT (up to ∼0.15°C) for ice drafts deeper than ∼250 m (Figure 6(d,f)); presumably due to inflows of warmer AW during that season. This results in a stronger melt driven circulation inside the cavity, which in turn,

https://doi.org/10.5194/egusphere-2023-73
Preprint. Discussion started: 27 January 2023

as a secondary effect, likely increases the u^* (up to ∼0.003 m/s) slightly downstream (∼80.6° to 80.9° N, ∼298.5° to 299.5° E) of the regions of the strongest seasonal warming (Figure 6(c,g,i)). The increased meltwater production/stronger melt driven overturning also brings more cold meltwater from depth to the shallower regions of the PGIS, which leads to a decrease in ΔT beneath the shallow ice during summer, and vice versa in winter (Figure 6(b,c,e,f,h,i)). Further, an increase in u^* beneath the shallow ice in winter could presumably relate to strengthening of the fjord circulation during that season (Figure 6(g,h)). These seasonal patterns are qualitatively similar for all runs (not shown here), with differences that arise due to changes in the sea ice cover investigated further in Sect. 3.2.1.

3.2 Ice Nudge Experiments - from *Thick Landfast* to *Thick Mobile* and *Thin Mobile*

3.2.1 Amplification of the PGIS basal melt

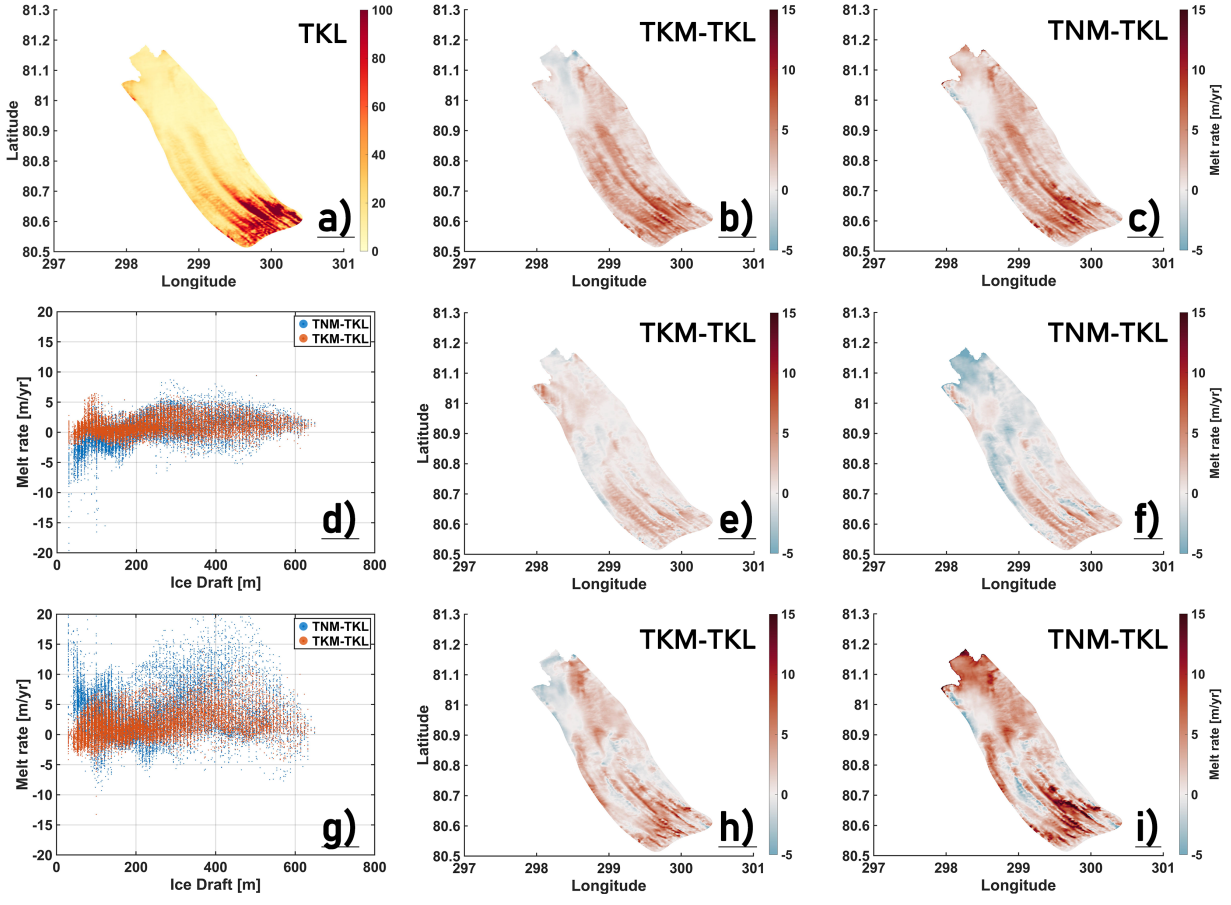

Figure 7. PGIS annual (2016) modelled mean melt rate for the *Thick Landfast* experiment (a), with the *Thick Mobile* (b) and the *Thin Mobile* (c) anomalies relative to it. Winter (d-f) and summer (g-i) modelled mean melt rate anomalies for the *Thick Mobile* and the *Thin Mobile* run shown relative to the *Thick Landfast* run; plotted vs. the ice draft (d,g) and as TKM-TKL (e,h) and TNM-TKL (f,i) anomaly maps.

https://doi.org/10.5194/egusphere-2023-73
Preprint. Discussion started: 27 January 2023

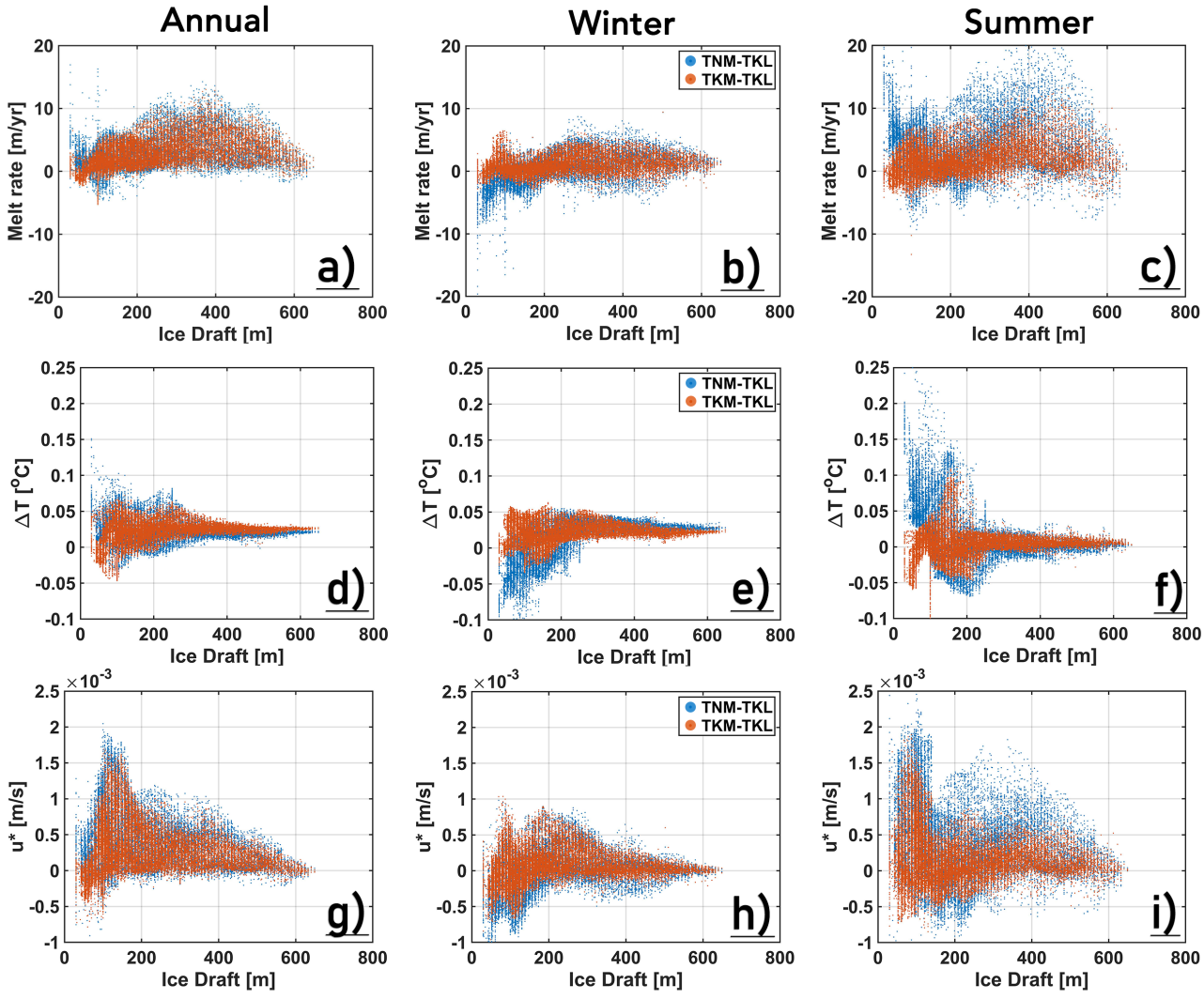

Figure 8. The *Thick Mobile* and *Thin Mobile* melt rate (a-c), thermal driving (ΔT) (d-f) and friction velocity (u^*) (g-i) anomalies shown relative to the *Thick Landfast* experiment. (a,d,g), (b,e,h) and (c,f,i) correspond respectively to the annual, winter and summer means.

To illustrate the amplification of the PGIS basal melt signal in response to the sea ice cover transitioning from *Thick Landfast* to *Thick Mobile* and *Thin Mobile*, annual and seasonal mean melt rate anomalies for the *Thick Mobile* and *Thin Mobile* runs with respect to the *Thick Landfast* run are shown (Figure 7). When transitioning from the *Thick Landfast* to the *Thick Mobile* scenario, the increase in annual mean modelled basal melt rates averaged over the entire PGIS area is $\sim$2.14 m/yr (Figure 7(a,b)), and where a stronger mean melt rate gain of $\sim$3.94 m/yr averaged over the deeper ($\geq$250 m) regions of the PGIS is observed. A strong seasonality is seen in the mean melt rate anomaly signals, with considerably higher mean melt rate gains during summer as compared to winter (Figure 7(d,e,g,h)). Further, irrespective of the season, stronger mean melt rate gains are observed near the deeper regions of the PGIS base close to the GL, with an increase in the winter (summer) mean melt rate

https://doi.org/10.5194/egusphere-2023-73
Preprint. Discussion started: 27 January 2023

anomalies averaged over the deeper regions of ∼5.4 m/yr (∼6.6 m/yr). Transitioning further to a thin, mobile sea ice regime results in an additional increase of ∼0.33 m/yr in the area averaged annual mean basal melt rates (Figure 7(c)). Here, the annual mean melt rate averaged over the deeper regions of the ice shelf shows a further increase of up to ∼0.12 m/yr. The summer mean melt rate gains greatly exceed that of winter, where substantial increases are observed near the GL, and also near the PGIS calving front (Figure 7(d,f,g,i)), while for winter, changes in the deeper regions are mixed with nominal melt rate gains and a decrease in shallow melt near the calving front (see below). Calculations show that for the deeper regions, the winter (summer) mean melt increases by an additional ∼0.13 m/yr (∼1.8 m/yr) as the sea ice regime, in addition to being mobile, becomes thin.

Changes in ΔT and u^* are used to further investigate the drivers of these changes in the basal melt (Figure 8). During summer, in both the *Thick Mobile* and *Thin Mobile* runs, ΔT does not change significantly for the PGIS draft deeper than ∼250 m (Figure 8(f)), and relative increases in ΔT are lower when compared to the corresponding winter anomalies (Figure 8(e)). Here, the increase in melt beneath the deeper regions of the PGIS base (Figure 8(c)) is primarily driven by the strengthening of the fjord circulation (see Sect. 3.2.3 and 4.2.3), as this increases the melt rate by enhancing the turbulent mixing (u^*) at the ice shelf base (Figure 8(i)). Further, the *Thin Mobile* run shows a decreased (increased) melt of shallower ice in winter (summer) (Figure 8(b,c)) due to the additional heat loss (gain) to (from) the atmosphere during the respective seasons under a thin sea ice cover (Figure 8(e,f), see Sect. 3.2.2 and 4.2.1).

3.2.2 Changes in water mass properties in the Nares Strait and PF

To investigate changes in water mass properties in PF in response to a changing sea ice cover, seasonal mean temperature and salinity differences along a transect over the PGIS cavity and the PF are shown in Figure 9, when transitioning from the *Thick Landfast* to the *Thick Mobile* and *Thin mobile* regimes.

Irrespective of the season, transitioning from a *Thick Landfast* sea ice cover to a *Thick Mobile* one results in an increase in temperature and salinity in the entire PGIS cavity (Figure 9(a,c,e,g)). In winter, the relative increase in salinity is less compared to summer (Figure 9(c,g)), however, we see a considerably higher increase in temperatures under the deeper regions of the PGIS base (Figure 9(a,e)). Up to ∼0.12°C warmer water masses are seen under the PGIS base seaward of the inner sill (draft $\leq$ 200 m), and which are ∼0.07 (∼0.12) psu saltier during winter (summer). Under the deeper PGIS base, winter heat (salt) gains are up to ∼0.1°C (∼0.04 psu), whereas in summer, those are up to ∼0.05°C (∼0.08 psu). With a regime characterized by *Thin Mobile* sea ice instead of a *Thick Mobile* one, nominal heat and salt gains (up to ∼0.01 in magnitude) are modelled for the deeper water masses in the outer basin, and in the inner PGIS basin during winter (Figure 9(b,d)). Strong upper ocean heat loss (up to ∼0.05°C colder) and salt gains (up to ∼0.14 psu) are modelled seaward of the calving front. The colder water masses are advected into the PGIS cavity, where anomalies of up to ∼0.04°C are seen (see further below). In summer, shortwave melting of the local sea ice in the fjord results in considerable freshening of the upper ocean and the shortwave heated (near) surface waters are seen to encroach under the outer shallower regions of the ice shelf base (Figure 9(f,h)). Up to ∼0.2°C warmer waters are seen to contact the shallower (<100 m) regions of the PGIS base near the calving front (Figure 9(f)), with positive heat anomalies of ∼0.08°C seen under the shallower (draft up to ∼250 m) PGIS base.

https://doi.org/10.5194/egusphere-2023-73
Preprint. Discussion started: 27 January 2023

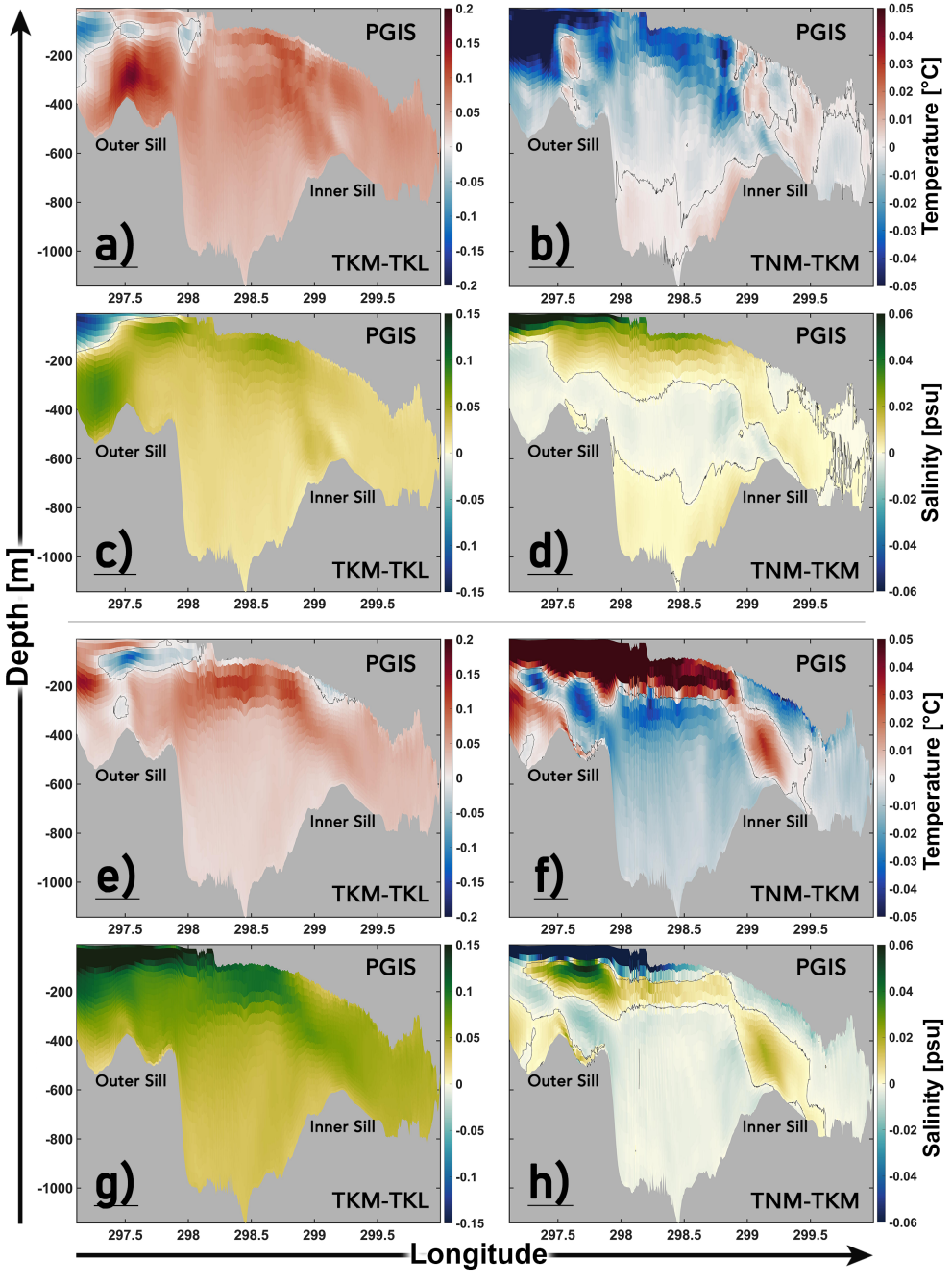

Figure 9. Mean temperature and salinity changes when transitioning between the numerical experiments, (Table 1). Anomalies are shown from the mouth of the PF (left panel margin), to the GL (right panel margin), cf. Figure 1(b) for profile location. Winter: Temperature: a) TKM-TKL, b) TNM-TKM. Salinity: c) TKM-TKL, d) TNM-TKM. Summer: Temperature: e) TKM-TKL, f) TNM-TKM. Salinity: g) TKM-TKL, h) TNM-TKM. Zero temperature and salinity difference contours shown in black. Note the different range of scales in each panel.

https://doi.org/10.5194/egusphere-2023-73
Preprint. Discussion started: 27 January 2023

These changes in the PGIS cavity and fjord are driven by changes in the ocean circulation in the fjord and the adjacent Nares Strait in response to the perturbed sea ice conditions. When the sea ice cover in the Nares Strait transitions from *Thick Landfast* to a *Thick Mobile* one (Figure 10(a,b)), a southward wind driven surface current in the Nares Strait causes a westward Ekman transport (consistent with findings reported in Shroyer et al., 2017, see further discussions in Sect. 4.2.2), wherein, the (cold and) fresh polar surface waters being displaced away from the Greenland (western) coast are replaced by the (warm and) saline AW at depth that are pulled up toward the Greenland coast. The AW being upwelled is warmer and more saline in summer as compared to winter (cf. Sect. 4.1.2, Figure 10(b)). Winter (summer) salt gains of up to ∼0.1 psu (up to ∼0.35 psu) are modelled in the upper ∼150-200 m of the water column along the Greenland coastline (Figure 10(a,b)). Similar salt gains seen in the fjord for both the seasons indicate that the upwelled AW from the adjacent Nares Strait enter the fjord and the PGIS cavity (see Figure 3 and Sect. 4.1.1; Figure 9(a,c,e,g)).

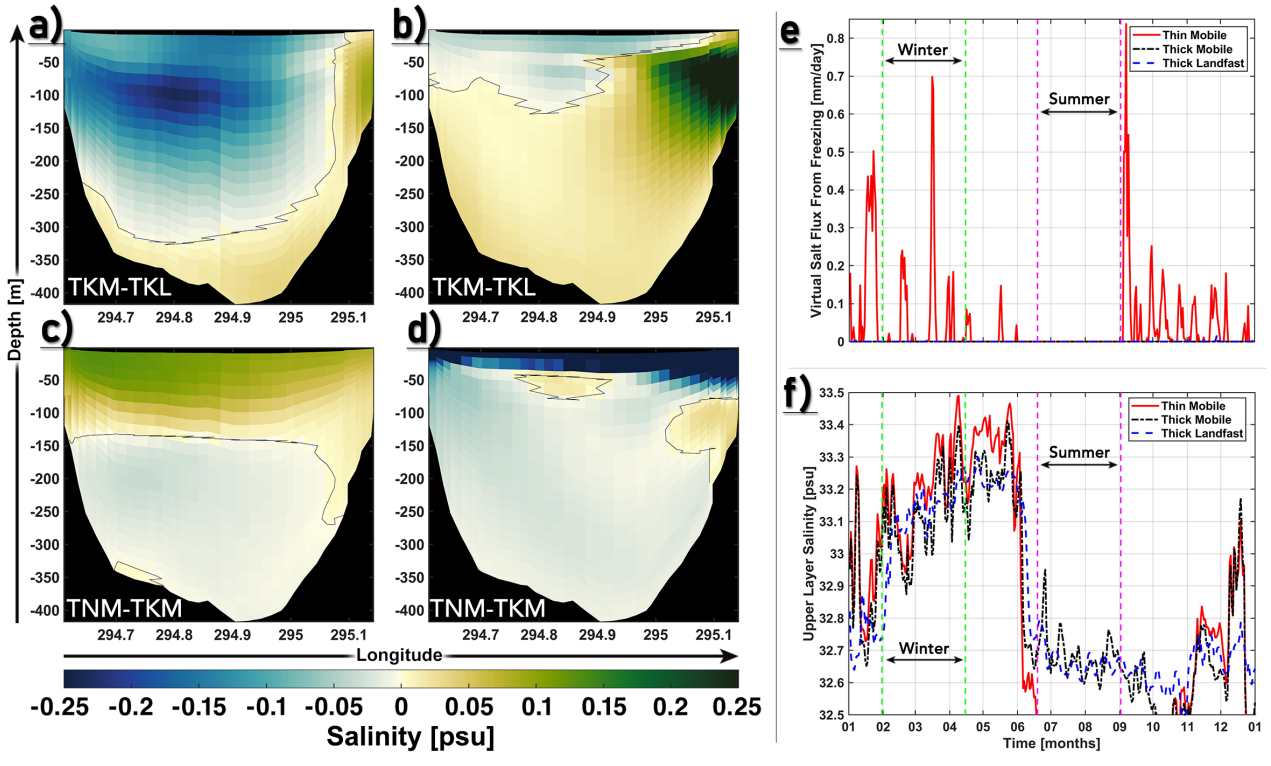

Figure 10. Seasonal mean salinity changes between the numerical experiments, see Table 1, across a section in the Nares Strait, south of PF, see Figure 1(b) for location. a) TKM-TKL, winter, b) TKM-TKL, summer. c) TNM-TKM, winter, d) TNM-TKM, summer. Black lines in panels a-d indicate the zero-salinity difference contour. Time series (2016), for runs TKL, TKM and TNM, of e) the virtual salt flux F_S due to sea ice freezing, and f) the upper layer salinity. Time series are shown for a node on the Nares Strait section near the eastern (Greenland) coastline. The dashed green and dashed magenta lines in panels e, f indicate the span of the winter and summer seasons, respectively.

When the sea ice cover (in addition to being mobile) becomes (negligibly) thin, latent heat loss resulting from strong atmospheric cooling during winter in the high Arctic over open ocean/thin ice supports a period of enhanced local sea ice

https://doi.org/10.5194/egusphere-2023-73
Preprint. Discussion started: 27 January 2023

production. Brine rejected during sea ice formation results in salinification of the upper ocean layer. The resulting loss of stratification destabilizes the water column and drives a thermohaline convection which allows further upwelling of the deeper lying AW (Figure 10(c,e,f)). An increase in salinity of up to ∼0.15 (∼0.05) psu is modelled in the upper ∼150 (250) m of the water column along the western (eastern) flank. Stronger salt gain towards the western flank (Figure 10(c)) suggests that sea ice formation on the eastern flank is (further) limited by the wind upwelled AW. At the onset of summer, owing to a warmer atmosphere, cessation of sea ice formation is seen (Figure 10(e)). Further, the heat gain drives enhanced sea ice melting resulting in significant freshening of near surface waters (Figure 10(d), Figure A2). Inside PF, during winter, it is likely that nominal heat and salt gains delivered by the convective overturning mechanism correspond to the warmer and saltier AW that overflow the outer sill and occupy the greater depths of the outer and inner fjord basin (Figure 9(b)), where they contribute to increases in ΔT, and thus, basal melt (Figure 8(b,e,h)). Also, heat loss and salt gains of comparable (to the Nares Strait section) magnitude driven by this mechanism are seen seaward of the calving front (Figure 9(b,d)). Confined largely to the shallower outer regions of the PGIS base (Figure 9(b)), the colder waters entering the cavity act to lower the ΔT and basal melt (Figure 8(b,e)).

3.2.3 Intensification of ocean circulation

As the sea ice cover becomes mobile and thin, another mechanism via which the heat transport in the PGIS cavity, and thereby, the basal melting is impacted is through the transfer of mechanical energy from air to sea. The resulting intensified flows increase the u^* that regulates the shear driven turbulent heat transfer across the ice shelf-ocean boundary (see discussions in Sect. 4.2.3, 4.2.4). Changes concerning the inflow into the PGIS cavity in response to the sea ice regime in the Nares Strait shifting from *Thick Landfast* to *Thick Mobile* and *Thin Mobile* are shown in Figure 11 (see below, and discussions in Sect. 4.2.3). Further, the heat budget of the PGIS cavity is extended to include the *Thick Mobile* and *Thick Landfast* experiments to investigate changes in the mean heat transport in response to a changing sea ice cover (see Table 2 and Sect. 4.2.3).

During winter, a strengthening of the inflow along the western fjord sector is modelled, which intensifies with depth (up to ∼0.03 m/s higher at depths of ∼700-800 m), as the sea ice regime changes from *Thick Landfast* to *Thick Mobile* (Figure 11(a)). There is a further increment in the inflow when transitioning from *Thick Mobile* to *Thin Mobile* conditions, with near surface currents, in the layers adjacent to the PGIS base in the western part of the PF, increasing by up to ∼0.02 m/s (Figure 11(b)).

During summer, when compared to winter, a similar strengthening of the inflow on the western sector of the fjord is modelled in response to prescribing the *Thick Mobile* instead of *Thick Landfast* sea ice conditions (Figure 11(a,c)). However, the strongest gains (up to ∼0.04 m/s) occur relatively higher up in the water column (at ∼300-400 m) and are associated with marginally higher magnitudes as compared to winter. Further, when prescribing a *Thin Mobile* sea ice regime instead of a *Thick Mobile* one, inflow through the western sector intensifies, predominantly along the western fjord wall where near-surface currents under the PGIS base are up to ∼0.08 m/s higher (Figure 11(d)). A strong weakening (up to ∼0.04 m/s) is seen in a narrow column along the western part of the fjord (depths of ∼400-600 m), however, the inflow is largely characterized by strong gains of up to ∼0.04 m/s across the western sector, with no indications of a weakened inflow on the eastern sector.

https://doi.org/10.5194/egusphere-2023-73
Preprint. Discussion started: 27 January 2023

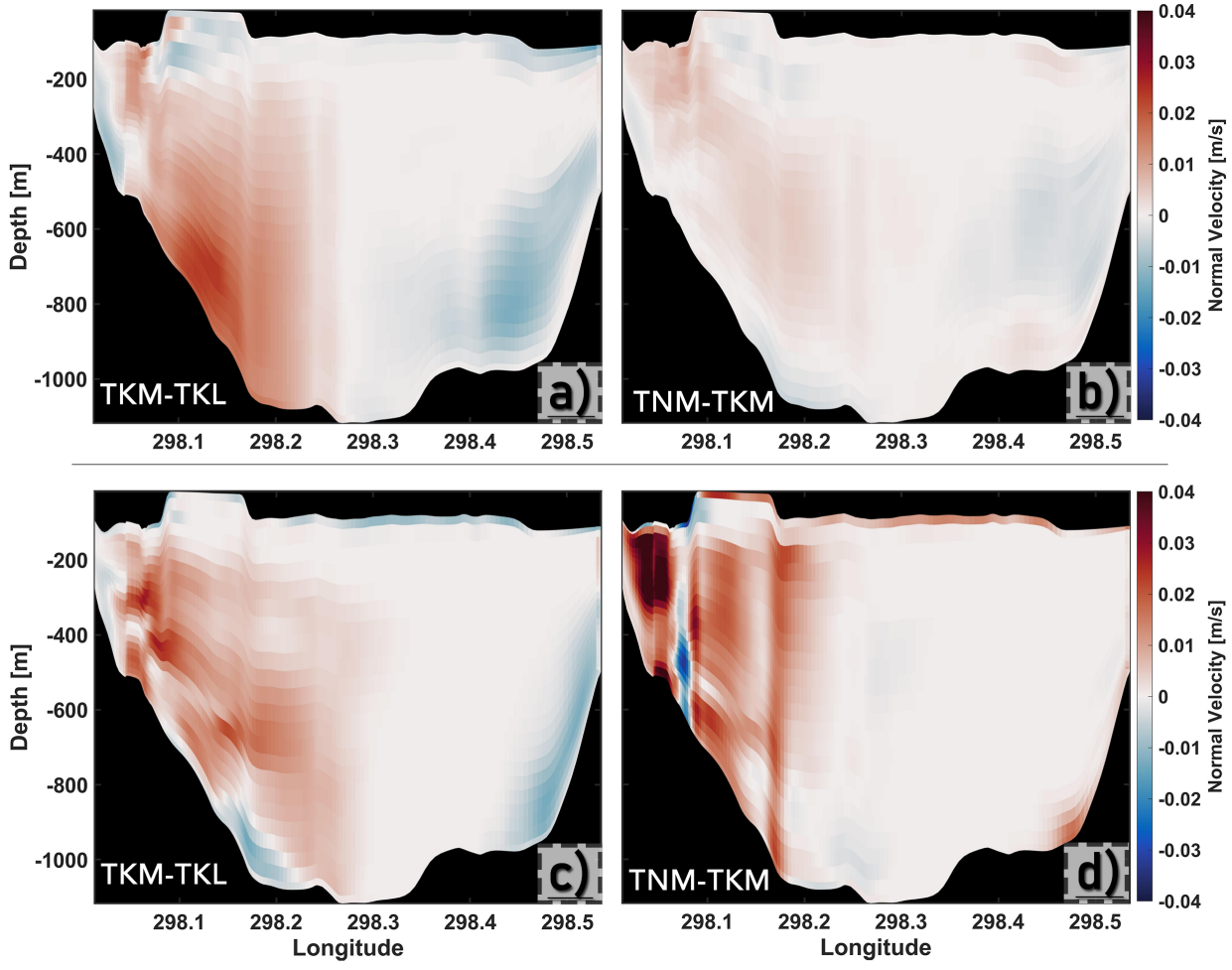

Figure 11. Inflow anomalies across the PGIS section shown in Figure 1(b), in response to the sea ice regime changing from *Thick Landfast* to *Thick Mobile* and *Thin Mobile*. Winter: a) TKM-TKL, b) TNM-TKM. Summer: c) TKM-TKL, d) TNM-TKM.

	TKL			***TKM***			***TNM***		
Field	Summer	Winter	Annual	Summer	Winter	Annual	Summer	Winter	Annual
H_{IN}	3.30	2.60	2.92	3.92	3.05	3.35	4.42	3.12	3.43
H_{OUT}	−2.81	−2.39	−2.58	−3.44	−2.83	−3.00	−3.88	−2.91	−3.06
H_{NET}	0.49	0.21	0.34	0.48	0.22	0.35	0.54	0.21	0.37

Table 2. Seasonal (summer, winter) and annual mean heat budget of the PGIS cavity and Fjord system for the *Thick Landfast* (TKL), *Thick Mobile* (TKM) and *Thin Mobile* (TNM) runs. H_{IN} and H_{OUT} (in TW), respectively, are the heat flux entering and leaving the PGIS cavity, and H_{NET} (in TW) is the sum of H_{IN} and H_{OUT}. Positive (negative) sign indicates that the flux of heat is directed into (out of) the PGIS cavity.

https://doi.org/10.5194/egusphere-2023-73
Preprint. Discussion started: 27 January 2023

4 Discussion

4.1 Thick Landfast Run

4.1.1 Depth averaged seasonal mean currents in the PF and the PGIS cavity

The modelled mean flow in summer is consistent with remotely sensed summer snapshots of the surface circulation from the Hall Basin and north of the PGIS calving front, which provided evidence of a general southward current in the Nares Strait, with a cross-strait component in the Hall Basin (Johnson et al., 2011). Furthermore, a similar (cyclonic) gyre was seen near the mouth of the PF, and also modelled by Shroyer et al. (2017) under a summer mobile sea ice cover. Figure 3 suggests that the lateral inflow (outflow) near the fjord mouth is directed equatorward (poleward) along the western (eastern) fjord wall (hence propagating like a Kelvin wave), and is also consistent with findings reported by Shroyer et al. (2017). In Figure 3, streamlines have only been presented for the *Thick Landfast* run. Counterparts for the *Thick Mobile* and *Thin Mobile* runs are presented in Figure A1. Bathymetry likely exerts a major control on the mean circulation prevailing in the PF (Figure 3), and it is thus speculated that circulation patterns would remain relatively similar, despite changes in sea ice regime. Indeed, Figure 3 and Figure A1 support this as modelled patterns are relatively similar across the three experiments and persist irrespective of season. Yet, they vary in magnitude, possibly in response to modulations in the air-sea momentum transfer induced by the varying sea ice cover regimes in the three experiments (Table 1, Figure 3, Figure A1, Sect. 4.2.3). It is therefore suggested that the exchange of water masses between the Nares Strait and the PF is maintained all year round which facilitates the renewal of water masses in the fjord. Further, the warm and saline AW that enter the PF at depth can be effectively circulated in the PGIS cavity and transported to the GL.

4.1.2 Seasonal mean normal flow across the outer sill and into the PGIS cavity

Under a year-round *Thick Landfast* sea ice regime in the Nares Strait, strengthening of the inflow of the warm and saline AW into the PGIS cavity during summer (cf. Figure 4) may be caused by a stronger melt driven overturning circulation when compared to winter (Figure 6). The AW that overflow the ∼350-443 m deep outer sill and fill the outer (∼1100 m deep) basin are ∼1.5°C (∼1.7°C) above the pressure melting point (∼ -2.3°C) at the GL depth during winter (summer) (Figure 4 (a,b)). As the summer AW at the GL depth are warmer (and denser) compared to winter, therefore, the stronger summer inflow events (Figure 4(a,b)) deliver larger volumes of warmer and saltier AW deep into the PGIS cavity.

Irrespective of the causes, one implication of a stronger inflow of warmer AW into the PGIS cavity in summer is higher melt at the PGIS base (see Figure 6(a-c), Sect. 4.1.3). Exact quantification of this melt is challenging, because AW temperatures modelled with A4, within which the PGIS setup in FVCOM is nested, exhibit a known cold-bias when compared to observations (Johnson et al., 2011, Heuzé et al., 2017, Washam et al., 2018, Jakobsson et al., 2020b, Prakash et al., 2022). To avoid cold-biased temperatures and an underestimation of basal melt, Prakash et al. (2022) implemented a scaling of the turbulent heat flux across the PGIS-ocean boundary which resulted in modelled melt rates that compare well with estimates reported by

https://doi.org/10.5194/egusphere-2023-73
Preprint. Discussion started: 27 January 2023

Wilson et al. (2017). Hence, it is assumed that modelled basal melt renders a fair quantification (under the assumption of a linear scaling to correct for a bias in the far field ocean temperatures), for the here presented numerical experiments.

Summer snapshots acquired during hydrographic surveys in the PF region provided evidence of a thick layer of PGIS meltwater, located in the ∼50-300 m depth range. This meltwater layer was reported to be bounded by cold and fresh polar surface waters above, and warm and dense AW below, as well as to leave the PF along its eastern part (Johnson et al., 2011; Heuzé et al., 2017). However, rich concentrations of PGIS meltwater were also found leaving the fjord from the western sector. Therefore, it is likely that the modelled outflow along the eastern fjord sector (Figure 4) transports much of the PGIS meltwater (not shown here) out of the fjord. The subsidiary summer outflow in the ∼50-250 m depth range on the western flank (Figure 4(d)) is also likely to export PGIS meltwater from enhanced melt along channels that run along the PGIS base, locally thinning it to ∼50-70 m in the central and western sectors near the calving front (Rignot and Steffen, 2008) (Sect. 4.1.3, Figure 6(a-c)).

4.1.3 Oceanic controls on the PGIS basal melt for the Thick Landfast run

To provide context for a discussion on the oceanic controls on the PGIS basal melt, heat fluxes directed into, and out of the PGIS cavity are discussed first. The model derived estimate of the summer mean H_{NET} of ∼0.49 TW (cf. Sect. 3.1.2) is comparable to the first order net heat flux estimates of ∼0.31 TW and ∼0.5 TW directed into the fjord provided by Johnson et al. (2011) and Heuzé et al. (2017), respectively. It is to be noted that the *Thick Landfast* run, with a fast ice cover during summer in the Nares Strait represents a conservative sea ice scenario as compared to the periods corresponding to the reported estimates (Kwok et al., 2010, Moore and McNeil, 2018). However, the reported estimates were deduced from summer snapshots of geostrophic velocities that did not span the entire width of the fjord, which could be a reason for the underestimation of reported H_{NET} when compared to the modelled one. Also, as no direct observations exist, particularly those that are representative of the mean (seasonal) states, further comparison between the modelled and observed net heat fluxes is not possible.

The thermal forcing in the PGIS cavity is strong enough to ensure that there is ample heat available to melt the PGIS base throughout the year, though with seasonal and spatial variation in both the AW θ-S signatures (Figure 5(a-f)) and the mean modelled basal melt rates (see Figure 6(a-c), Holland, 2017). The modelled (time) mean basal melt rates are strongly correlated to the depth and slope of the PGIS draft (for the model PGIS basal topography details, see Prakash et al. (2022)): higher melt is seen for regions characterized by deeper ice shelf draft and/or steeper PGIS basal slopes (Figure 6(a)), and is consistent with the spatial variability seen in the satellite derived estimates reported by Wilson et al. (2017). For instance, the ice shelf draft is deepest near the GL, particularly on the eastern sector with depths of ∼600 m, and where some of the steepest ice shelf basal slopes are found. Here, modelled mean basal melt rate exhibits large peaks (Figure 6(a)). Additionally, at deeper ice shelf drafts of ∼400-600 m, the seawater melting point is lowered (∼ -2.2 - -2.4°C) which enhances the thermal forcing. The mean thermal forcing is considerably higher during summer, based on the seasonal differences in θ near the GL. Further, sub-ice shelf channels resulting from channelized basal melting of the PGIS (Rignot and Steffen, 2008) have imposed steep transverse and longitudinal ice shelf thickness gradients which support stronger entrainment in the buoyant meltwater plumes. These channels are several km wide and extend along the length of the PGIS, deepening in the direction of the PGIS flow.

https://doi.org/10.5194/egusphere-2023-73
Preprint. Discussion started: 27 January 2023

Mean basal melt rates of up to ∼80 m/yr are estimated over the 2011-2015 period for the deepest regions of the PGIS (Wilson et al., 2017), however, they mostly range between ∼40-50 m/yr, decaying rapidly over a distance of ∼20 km seaward of the GL to ∼10 m/yr. Furthermore, between 23 August - 08 December, 2015, Washam et al. (2020) estimated area averaged basal melt rate maxima of ∼40-170 m/yr upstream of a location 16 km from the GL in the central basal channel, regulated by the buoyant subglacial discharge which produced strong sub-ice shelf currents. It is to be noted that the FVCOM setting for the PGIS used here does not feature subglacial discharge at the GL (to accelerate the sub-ice shelf currents). Further, there are inconsistencies between the model sea ice regime and period as compared to the reported estimates (cf. Table 1, Kwok et al., 2010, Moore and McNeil, 2018). Therefore, comparisons made here are qualitative in nature, however, it is to be noted that the novel mechanisms identified in this study, suggesting how changing sea ice conditions in the Nares Strait affect melting beneath the PGIS are robust, while other mechanisms such as melt rate increase through subglacial discharge needs to be considered in addition, when assessing the response of PGIS basal melt in a future climate. The annual mean modelled basal melt rates under the deeper regions of the PGIS base near the GL (Figure 6(a)) compares well with the estimates of Wilson et al. (2017), largely exhibiting values in the range of ∼50-80 m/yr, and decreasing rapidly to ∼10-40 m/yr at ∼20 km from the GL. Furthermore, the modelled summer mean basal melt rate maxima of ∼80 - ∼150 m/yr seen along the basal channels near the GL lies within the estimated limits provided by Washam et al. (2020) (Figure 6(a,c)).

4.2 Ice Nudge Experiments

The numerical experiments presented and discussed here are enabled by the *Ice Nudge* module in FVCOM, through which the sea ice mobility, thickness and extent are controlled (Table 1, Sect. 2.2). The experiments are designed to investigate changes at the PGIS that are induced by the loss of the *thick* and *landfast* sea ice cover, and associated increase in the frequency of winter sea ice arch collapses in the Nares Strait (Moore and McNeil, 2018; Moore et al., 2021).

4.2.1 Thermal implications of a TNM ice cover on the shallower PGIS basal melt

Modelled future Arctic sea ice projections predict a strong likelihood of having a sea ice free summer before 2050 CE (Wang and Overland, 2012; Notz and SIMIP Community, 2020). In such scenarios, with much of the oldest and thickest multi-year ice packs in the Arctic no longer present (Maslanik et al., 2011; Kwok, 2018; Kacimi and Kwok, 2022), ice arches would likely fail to form, resulting in a year round mobile and thin sea ice cover in the Nares Strait, with implications for PGIS basal melt, and therefore motivating our suite of experiments.

Recent satellite imagery has revealed new fractures on the PGIS, propagating from the eastern fjord wall towards the west, and located at ∼40 km from the GL (∼10 km landward from the recent front position), signaling a likely large calving event in the near future (Rückamp et al., 2019). Under a *Thin Mobile* sea ice cover, besides changes in the summer u^* (see Figure 8(i), Sect. 4.2.3) and the convectively upwelled AW during winter (Figure 8(e)) that drive the basal melting under the deeper regions of the PGIS base, the substantial increase in ΔT near the PGIS calving front due to shortwave warming over open ocean (Figure 8(f)) could have serious implications for enhanced melt driven undercutting and glacier calving in the (near) future as the Arctic sea ice continues to decline in extent and thickness.

https://doi.org/10.5194/egusphere-2023-73
Preprint. Discussion started: 27 January 2023

4.2.2 Upwelled AW in the Nares Strait and PF, and the importance of sub ice shelf bathymetry

The continued warming of the Nares Strait AW (Washam et al., 2018; Jakobsson et al., 2020b), could, on a wider scale, likely be attributed to warming of the Arctic Ocean, which is modelled to continue until the end of the 21st century (Shu et al., 2022). The presence of a considerably warmer AW in the future is likely to amplify the heat delivered by the upwelling mechanisms. Additionally, under a *Thin Mobile* sea ice regime in winter, the higher (upwelled) vertical heat flux will result in an increased (basal) sea ice melt, sustaining and/or creating more regions of thin sea ice/open ocean, and thereby sustaining the convectively overturned upwelling of the warmer AW.

Wind driven upwelling of AW in the Nares Strait in response to a mobile summer sea ice forcing was previously modelled by Shroyer et al. (2017), however, its effect was restricted to the shallower ($\leq$200 m) regions of the PGIS, rather than extending to greater (up to $\sim$600 m) depths, as in the here modelled scenario(s) (see Figure 9). It can be argued that such a discrepancy arises due to an unrealistic ice shelf basal topography, and more importantly, an inaccurate sub ice shelf bathymetry derived from the BedMachine v3 dataset implemented in the model setup used by Shroyer et al. (2017). Indeed, Prakash et al. (2022) showed that the BedMachine v3 water column thickness under the deeper ($>$200 m) regions of the PGIS are negligibly thin ($\sim$0-50 m on either flanks, and $\sim$50 - 100 m under the central zone), which is not a realistic representation of the actual sub PGIS topography. Hence, an artificial, shallow ($\sim$250-300 m) sill would hinder any warmer AW at depth (see Figure 5(a-f)) from reaching the deeper regions of the PGIS cavity in the inner basin in Shroyer et al. (2017), but not in Prakash et al. (2022) where the shortcomings in the BedMachine v3 dataset were accounted for (see Sect. 2.1, Sect. 4.1.1).

4.2.3 Intensification of ocean circulation

Results from the numerical experiments (Table 1) designed to capture the impacts of changing sea ice regimes in the Nares Strait on the PGIS support the notion that wind driven intensification of ocean circulation results in an increased inflow into the PGIS cavity (Figure 11). Moreover, appearance of large areas of open ocean in the Nares Strait and PF in the *Thin Mobile* run during summer (see Figure 2(b,e)) further intensifies the inflow (Figure 11(d)). This acts to greatly enhance the u^* at the ice shelf-ocean boundary, and is also the prominent driver of basal melting at the deeper regions of the ice shelf base (Figure 8(c,f,i)). Between 1996-2002, landfast sea ice cover prevailed in the Nares Strait for $\sim$7-10 months each year following the formation of southern or both northern and southern ice arches Kwok et al. (2010). There is also a strong agreement between the model winter and summer fast ice periods (cf. Table 1) and the estimates of ice flux stoppage duration reported in Kwok et al. (2010). Particularly, estimates from the period 1998-2001 support the hypothesis of a fast ice cover during the model winter and summer seasons. Additionally, estimates from the period 1996-1998 show fast ice over the (model) summer season with $\sim$1 month overlap during (model) winter, and vice versa for the 2001-2002 estimate. Therefore, it can be argued that the *Thick Landfast* experiment setup, and as such, the contrasting results presented here for the *Thick Mobile* and the *Thin Mobile* runs with respect to it, are plausible. To that end, the wind driven winter (summer) inflow directed into the PGIS cavity is increased by $\sim$13% ($\sim$22%) in the presence of a mobile sea ice cover, and additionally by $\sim$4% ($\sim$15%) in the presence of a (negligibly) thin sea ice cover.

https://doi.org/10.5194/egusphere-2023-73
Preprint. Discussion started: 27 January 2023

Changes in inflow and temperature are interpreted to alter the heat budget in the PGIS cavity, impacting basal melt (Sect. 4.2.4): The increase in winter (summer) heat inflow (H_{IN}, see Table 2) driven by the collective gains in temperature and current (Sect. 3.2.2, 3.2.3) is ∼17% (∼19%) when the sea ice becomes mobile, and a further ∼2% (∼13%) when it becomes (negligibly) thin. Similar to the *Thick Landfast* run, summer H_{IN} is substantially higher than winter H_{IN} for both the *Thick Mobile* and *Thin Mobile* runs, with much of the H_{IN} leaving the cavity (H_{OUT}) without triggering any basal melt (Table 2).

4.2.4 Amplification of the PGIS basal melt

The PGIS basal melt increases in the *Thick Mobile* and the *Thin Mobile* runs (Figure 7) because the surface forcing modulations increase the heat transport into the cavity (Table 2) through a combined effect of higher temperature (Figure 9) and enhanced transport (Figure 11). Temperature increase in the ice shelf cavity and fjord from wind driven upwelling (Figure 9(a,e)) is considerably higher than convective upwelling (Figure 9(b)), and is therefore regarded as the dominant (out of the two) surface forcing mechanism that drives basal melting at the PGIS (Figure 7). The contribution of the collective increase in temperature delivered by these mechanisms to the PGIS basal melt is further amplified by the wind driven intensification of circulation in the PGIS cavity, which increases the u^* in the absence of a (landfast and thick) sea ice cover (Figure 11), particularly during the summer season, in the deeper regions of the PGIS base, where more efficient melting is modelled in a more turbulent cavity, without necessarily an increase in ΔT.

5 Summary and concluding remarks

Here, we have presented results, showing in unprecedented detail, the impact of changing Nares Strait sea ice regimes following the loss of stabilizing ice arches on the basal melt at Petermann Glacier Ice Shelf (PGIS), North-West Greenland. Results were obtained using the unstructured grid, free-surface, 3-D primitive equation Finite Volume Community Ocean Model, FVCOM, which was amended by a new Ice Nudge module and adapted to render a nested high resolution 3-D ocean-sea ice-ice shelf setup for the PGIS and Petermann Fjord (PF). Analysing and comparing the different sea ice cover scenarios, we find the following:

- *Persistent mean circulation patterns in the PF irrespective of the season and the sea ice regime:* Modulations in the air-sea momentum flux driven by sea ice regime changes from *Thick Landfast* to *Thick Mobile* and *Thin Mobile* are discernable in the vertically averaged seasonal mean (ocean) speed signals. However, regardless of the applied surface forcing, the corresponding circulation patterns in the fjord remain similar. This suggests that the bathymetry in PF likely exerts a major control on the mean circulation. To that end, it is evident that the exchange between the PF and the Nares Strait persists irrespective of the season and/or the sea ice regime.

- *Seasonal and spatial variability of the melt rate drivers and basal melt:* A warmer Atlantic water (AW) during summer increases the thermal driving (ΔT) for the deeper ($\sim$ >250 m) ice drafts, resulting in stronger melt driven overturning which then increases the friction velocity (u^*) slightly downstream of the regions where ΔT is strongest. Further, larger

https://doi.org/10.5194/egusphere-2023-73
Preprint. Discussion started: 27 January 2023

meltwater transports from depth to the shallower regions act to reduce ΔT and the basal melt. Winter season exhibits a converse behaviour, and these seasonal patterns are qualitatively similar irrespective of the sea ice regime in place.

- *PGIS basal melt amplification:* The increase in annual mean melt rate averaged over the entire PGIS base is ∼2.14 m/yr in the absence of a landfast sea ice cover, and a further ∼0.33 m/yr in the absence of a thick sea ice cover. Further, irrespective of the season, stronger melt rate gains are seen under the deeper areas of the PGIS near the grounding line (GL). Here, in the absence of a landfast sea ice cover, winter (summer) mean melt rate gains of ∼5.4 m/yr (∼6.6 m/yr) are seen, and further, in the absence of a thick sea ice cover, additional increase of ∼0.13 m/yr (∼1.8 m/yr) are seen.

- *Catalysts for the melt rate drivers:* As the sea ice becomes *mobile* and *thin*, changes in surface forcing act to enhance the ΔT and the frictional velocity (u^*) in the PGIS cavity, and thereby, the basal melt. Transitioning from a *Thick Landfast* to *Thick Mobile* sea ice regime uncovers the twofold contribution of wind: Thermodynamically, the wind upwelled AW from the adjacent Nares Strait enter the PGIS cavity. Mechanically, the wind driven fjord scale circulation strengthens, enhancing the turbulent heat exchange at the ice shelf-ocean interface. Additionally, when the sea ice cover thins, salt released during sea ice formation in winter drives a thermohaline convection which results in further upwelling of the AW. A further strengthening of the circulation is seen, particularly during summer as vast areas of open ocean appear.

- *Implications of increase in inflow and temperature to the PGIS basal melt:* The aggregate increase in temperature and current act in concert to increase the heat transport in the PGIS cavity in the *Thick Mobile* and the *Thin Mobile* runs. Temperature increase from wind driven upwelling is considerably higher compared to convective upwelling, and is therefore the dominant mechanism. For the deeper ice drafts, ΔT does not vary considerably in both the mobile runs (compared to the *Thick Landfast* run) during summer, while a substantial increase is seen during winter. The increase in temperature in the PGIS cavity in both the mobile runs due to upwelling of warmer AW in summer act to enhance the strong summer thermal forcing, particularly at greater depths near the GL, and therefore, the basal melt. The increased meltwater production likely results in the relatively lower gains that are seen in ΔT, and further, drives a stronger melt overturning which together with the wind intensified currents in the cavity, particularly for the *Thin Mobile* run, increase the u^* at the ice shelf base, which is the dominant driver of basal melting. Additionally, strong upper open ocean heat gain (loss) creeps under the shallower outer regions of the ice shelf base during summer (winter). While the colder/lower ΔT acts to lower the melt, the strong shortwave warming results in strong basal melt.

Remotely sensed and in-situ observations over the past two decades from the Lincoln Sea - Nares Strait region provide evidence for sustained increase in ocean temperatures and a continued decline of ice stoppage duration aided by the collapse/absence of ice arches which are becoming increasingly common. As warming of the Arctic Ocean and decline of its sea ice coverage and thickness is projected to continue until the end of the 21st century, the scenario presented in the *Thin Mobile* run is likely to continue in the future, and may amplify further. Its impact on the long term stability of the PGIS in the context of surface forced mechanisms is twofold: a) Heat supply: Here, heat delivered by the upwelling mechanisms in the PGIS cavity is likely to be amplified further. A warmer upwelled AW, in addition to increasing the PGIS basal melt, will enhance the sea

https://doi.org/10.5194/egusphere-2023-73
Preprint. Discussion started: 27 January 2023

ice basal melt, sustaining and/or creating more regions of open ocean, further enhancing the ice shelf basal melt. Also, stronger summer shortwave heating of the near surface fjord waters that encroach under the PGIS front will have implications for melt driven undercutting and calving. b) Currents: As the sea ice cover dwindles and more areas of open ocean appear in the Nares Strait and the PF, wind driven strengthening of fjord circulation (illustrated by the summer *Thin Mobile* run) will amplify. Amplifications seen in (a) and/or (b) will further amplify the basal melt rates, impacting the long term stability of the PGIS and its contribution to the future GrIS mass loss and sea level rise.

Code and data availability. The open source code Finite Volume Community Ocean Model version 4.0 (FVCOM4.0) that has been augmented to allow the inclusion of static ice shelf cavities is available from Zhou and Hattermann (2020) (doi.org/10.17632/m6g4c3hm9m.1). The Ice Nudge module is as described in Prakash et al. (2022). All model input files that are required to run the experiments are freely available to everyone, upon request.

https://doi.org/10.5194/egusphere-2023-73
Preprint. Discussion started: 27 January 2023

Appendix A: Supplementary Figures

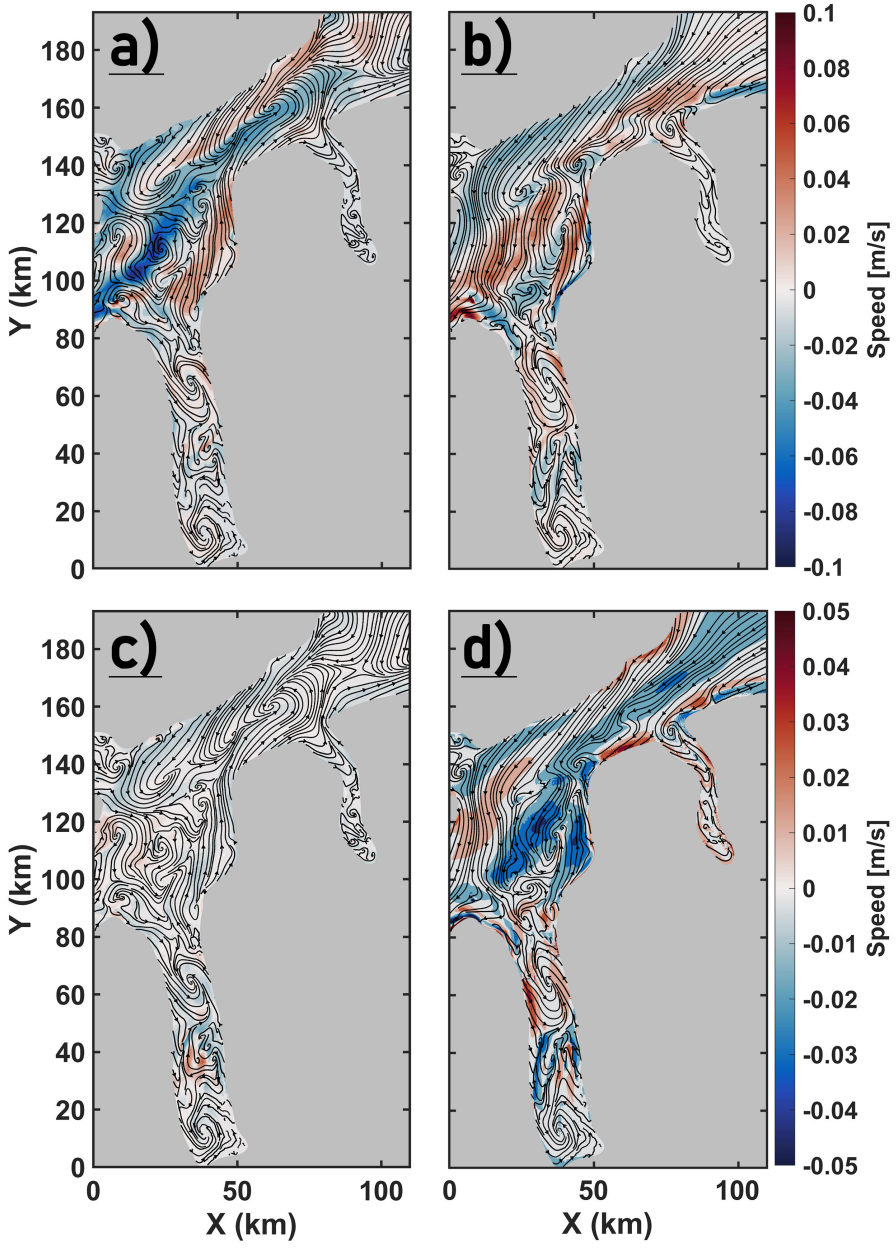

Figure A1. Depth averaged seasonal mean speed anomalies for the area indicated in Figure 1 (b), in response to the sea ice regime changing from *Thick Landfast* to *Thick Mobile* and *Thin Mobile*. Seasonal mean streamlines for the *Thick Mobile* and *Thin Mobile* experiments are overlaid as indicated below. a) Speed: TKM - TKL, Winter; Streamline: TKM, Winter. b) Speed: TKM - TKL, Summer; Streamline: TKM, Summer. c) Speed: TNM - TKM, Winter; Streamline: TNM, Winter. d) Speed: TNM - TKM, Summer; Streamline: TNM, Summer.

https://doi.org/10.5194/egusphere-2023-73
Preprint. Discussion started: 27 January 2023

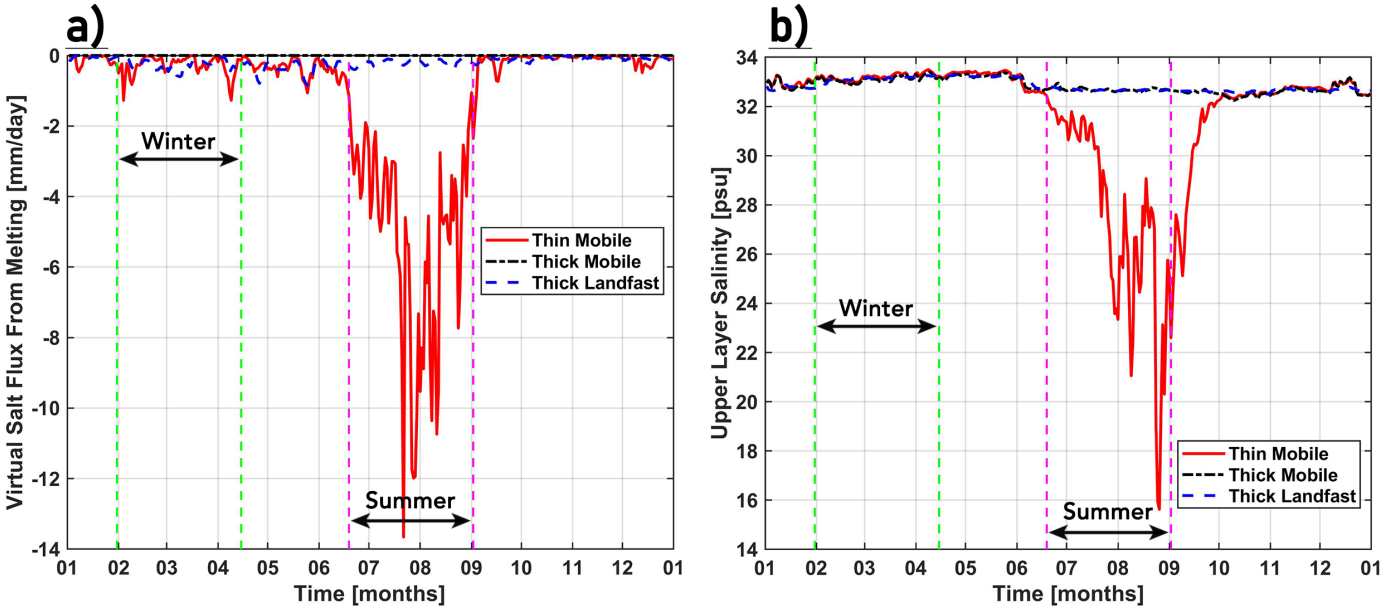

Figure A2. Time series (2016) of (a) the virtual salt flux due to sea ice melting, and (b) the upper layer salinity for the *Thick Landfast*, *Thick Mobile* and *Thin Mobile* runs. Note that a negative salt flux from sea ice melting (panel a) indicates a positive freshwater flux. The upper layer salinity (panel b) is zoomed out from Figure 10 (f) to show the strong summer freshening for the *Thin Mobile* run. The dashed green and magenta lines in both panels indicate the span of the winter and summer seasons, respectively. The time series in both panels is shown for the same node on the Nares Strait section near the Greenland coastline as Figure 10 (f).

Author contributions. AP conceptualised the study, and together with QZ and TH, designed the framework for the *Ice Nudge* experiments. AP ran the simulations, and interpreted the model output with advice from QZ and TH. AP carried out the model analysis with supervision from TH. AP and NK wrote the manuscript with contributions from QZ and TH.

Competing interests. None of the authors have any competing interests.

Acknowledgements. The work is funded by the Swedish Research Council FORMAS under grant 2017-00665 to Nina Kirchner and is also associated with the Research Council of Norway (RCN) project No. 280727 (PI: Rune Grand Graversen). Qin Zhou is supported by the RCN project Nos. 244319 and 295075. TH is supported by the RCN project No. 314570. The simulations were performed on resources provided by UNINETT Sigma2 - the National Infrastructure for High Performance Computing and Data Storage in Norway. The supercomputers Fram, Betzy and the NIRD storage facilities were used under the projects NN9348K, NN9824K and NS9063K, respectively.

https://doi.org/10.5194/egusphere-2023-73
Preprint. Discussion started: 27 January 2023

References

Aschwanden, A., Fahnestock, M. A., Truffer, M., Brinkerhoff, D. J., Hock, R., Khroulev, C., Mottram, R., and Khan, S. A.: Contribution of the Greenland Ice Sheet to sea level over the next millennium, Science advances, 5, eaav9396, 2019.

Chen, C., Huang, H., Beardsley, R. C., Liu, H., Xu, Q., and Cowles, G.: A finite volume numerical approach for coastal ocean circulation studies: Comparisons with finite difference models, Journal of Geophysical Research: Oceans, 112, 2007.

Chen, X., Zhang, X., Church, J. A., Watson, C. S., King, M. A., Monselesan, D., Legresy, B., and Harig, C.: The increasing rate of global mean sea-level rise during 1993–2014, Nature Climate Change, 7, 492–495, 2017.

Falkner, K. K., Melling, H., Münchow, A. M., Box, J. E., Wohlleben, T., Johnson, H. L., Gudmandsen, P., Samelson, R., Copland, L., Steffen, K., et al.: Context for the recent massive Petermann Glacier calving event, Eos, Transactions American Geophysical Union, 92, 117–118, 2011.

Hattermann, T., Isachsen, P. E., von Appen, W.-J., Albretsen, J., and Sundfjord, A.: Eddy-driven recirculation of Atlantic water in Fram Strait, Geophysical Research Letters, 43, 3406–3414, 2016.

Heuzé, C., Wåhlin, A., Johnson, H. L., and Münchow, A.: Pathways of meltwater export from Petermann Glacier, Greenland, Journal of Physical Oceanography, 47, 405–418, 2017.

Hill, E. A., Carr, J. R., and Stokes, C. R.: A review of recent changes in major marine-terminating outlet glaciers in Northern Greenland, Frontiers in Earth Science, 4, 111, 2017.

Hill, E. A., Carr, J. R., Stokes, C. R., and Gudmundsson, G. H.: Dynamic changes in outlet glaciers in northern Greenland from 1948 to 2015, The Cryosphere, 12, 3243–3263, 2018.

Holland, P. R.: The transient response of ice shelf melting to ocean change, Journal of Physical Oceanography, 47, 2101–2114, 2017.

Hunke, E. C., Lipscomb, W. H., Turner, A. K., Jeffery, N., and Elliott, S.: Cice: the los alamos sea ice model documentation and software user's manual version 4.1 la-cc-06-012, T-3 Fluid Dynamics Group, Los Alamos National Laboratory, 675, 500, 2010.

Jakobsson, M., Mayer, L. A., Bringensparr, C., Castro, C. F., Mohammad, R., Johnson, P., Ketter, T., Accettella, D., Amblas, D., An, L., et al.: The international bathymetric chart of the Arctic Ocean version 4.0, Scientific data, 7, 1–14, 2020a.

Jakobsson, M., Mayer, L. A., Nilsson, J., Stranne, C., Calder, B., O'Regan, M., Farrell, J. W., Cronin, T. M., Brüchert, V., Chawarski, J., et al.: Ryder Glacier in northwest Greenland is shielded from warm Atlantic water by a bathymetric sill, Communications Earth & Environment, 1, 1–10, 2020b.

Johnson, H., Münchow, A., Falkner, K., and Melling, H.: Ocean circulation and properties in Petermann Fjord, Greenland, Journal of Geophysical Research: Oceans, 116, 2011.

Kacimi, S. and Kwok, R.: Arctic Snow Depth, Ice Thickness, and Volume From ICESat-2 and CryoSat-2: 2018–2021, Geophysical Research Letters, 49, e2021GL097 448, 2022.

Kwok, R.: Variability of Nares Strait ice flux, Geophysical Research Letters, 32, 2005.

Kwok, R.: Arctic sea ice thickness, volume, and multiyear ice coverage: losses and coupled variability (1958–2018), Environmental Research Letters, 13, 105 005, 2018.

Kwok, R., Toudal Pedersen, L., Gudmandsen, P., and Pang, S.: Large sea ice outflow into the Nares Strait in 2007, Geophysical Research Letters, 37, 2010.

Maslanik, J., Stroeve, J., Fowler, C., and Emery, W.: Distribution and trends in Arctic sea ice age through spring 2011, Geophysical Research Letters, 38, 2011.

https://doi.org/10.5194/egusphere-2023-73
Preprint. Discussion started: 27 January 2023

Meredith, M., Sommerkorn, M., Cassotta, S., Derksen, C., Ekaykin, A., Hollowed, A., Kofinas, G., Mackintosh, A., Melbourne-Thomas, J., Muelbert, M. M. C., Ottersen, G., Pritchard, H., and Schuur, E. A. G.: Polar Regions, in: IPCC Special Report on the Ocean and Cryosphere in a Changing Climate, edited by Pörtner, H.-O., Roberts, D. C., Masson-Delmotte, V., Zhai, P., Tignor, M., Poloczanska, E., Mintenbeck, K., Alegría, A., Nicolai, M., Okem, A., Petzold, J., Rama, B., and Weyer, N. M., p. 203–320, Cambridge University Press, Cambridge, United Kingdom and New York, NY, USA, https://doi.org/10.1017/9781009157964.005, 2019.

Moore, G. and McNeil, K.: The early collapse of the 2017 Lincoln Sea ice arch in response to anomalous sea ice and wind forcing, Geophysical Research Letters, 45, 8343–8351, 2018.

Moore, G., Howell, S., Brady, M., Xu, X., and McNeil, K.: Anomalous collapses of Nares Strait ice arches leads to enhanced export of Arctic sea ice, Nature communications, 12, 1–8, 2021.

Morlighem, M., Williams, C. N., Rignot, E., An, L., Arndt, J. E., Bamber, J. L., Catania, G., Chauché, N., Dowdeswell, J. A., Dorschel, B., et al.: BedMachine v3: Complete bed topography and ocean bathymetry mapping of Greenland from multibeam echo sounding combined with mass conservation, Geophysical research letters, 44, 11–051, 2017.

Mouginot, J., Rignot, E., Bjørk, A. A., Van den Broeke, M., Millan, R., Morlighem, M., Noël, B., Scheuchl, B., and Wood, M.: Forty-six years of Greenland Ice Sheet mass balance from 1972 to 2018, Proceedings of the national academy of sciences, 116, 9239–9244, 2019.

Münchow, A.: Volume and freshwater flux observations from Nares Strait to the west of Greenland at daily time scales from 2003 to 2009, Journal of Physical Oceanography, 46, 141–157, 2016.

Münchow, A., Padman, L., and Fricker, H. A.: Interannual changes of the floating ice shelf of Petermann Gletscher, North Greenland, from 2000 to 2012, Journal of Glaciology, 60, 489–499, 2014.

Noël, B., van de Berg, W. J., Lhermitte, S., and van den Broeke, M. R.: Rapid ablation zone expansion amplifies north Greenland mass loss, Science advances, 5, eaaw0123, 2019.

Notz, D. and SIMIP Community: Arctic sea ice in CMIP6, Geophysical Research Letters, 47, e2019GL086 749, 2020.

Padman, L. and Erofeeva, S.: A barotropic inverse tidal model for the Arctic Ocean, Geophysical Research Letters, 31, 2004.

Pörtner, H.-O., Roberts, D. C., Masson-Delmotte, V., Zhai, P., Tignor, M., Poloczanska, E., and Weyer, N.: The ocean and cryosphere in a changing climate, IPCC Special Report on the Ocean and Cryosphere in a Changing Climate, 2019.

Prakash, A., Zhou, Q., Hattermann, T., Bao, W., Graversen, R., and Kirchner, N.: A nested high-resolution unstructured grid 3-D ocean-sea ice-ice shelf setup for numerical investigations of the Petermann ice shelf and fjord, MethodsX, 9, 101 668, 2022.

Rignot, E. and Steffen, K.: Channelized bottom melting and stability of floating ice shelves, Geophysical Research Letters, 35, 2008.

Rückamp, M., Neckel, N., Berger, S., Humbert, A., and Helm, V.: Calving induced speedup of Petermann glacier, Journal of Geophysical Research: Earth Surface, 124, 216–228, 2019.

Ryan, P. A. and Münchow, A.: Sea ice draft observations in N ares S trait from 2003 to 2012, Journal of Geophysical Research: Oceans, 122, 3057–3080, 2017.

Sasgen, I., Wouters, B., Gardner, A. S., King, M. D., Tedesco, M., Landerer, F. W., Dahle, C., Save, H., and Fettweis, X.: Return to rapid ice loss in Greenland and record loss in 2019 detected by the GRACE-FO satellites, Communications Earth & Environment, 1, 1–8, 2020.

Shroyer, E. L., Padman, L., Samelson, R., Münchow, A., and Stearns, L. A.: Seasonal control of Petermann Gletscher ice-shelf melt by the ocean's response to sea-ice cover in Nares Strait, Journal of Glaciology, 63, 324–330, 2017.

Shu, Q., Wang, Q., Årthun, M., Wang, S., Song, Z., Zhang, M., and Qiao, F.: Arctic Ocean Amplification in a warming climate in CMIP6 models, Science advances, 8, eabn9755, 2022.

https://doi.org/10.5194/egusphere-2023-73
Preprint. Discussion started: 27 January 2023

Slater, D. A., Straneo, F., Felikson, D., Little, C. M., Goelzer, H., Fettweis, X., and Holte, J.: Estimating Greenland tidewater glacier retreat driven by submarine melting, The Cryosphere, 13, 2489–2509, 2019.

The IMBIE Team: Mass balance of the Greenland Ice Sheet from 1992 to 2018, Nature, 579, 233–239, https://doi.org/10.1038/s41586-019-1855-2, 2020.

Tinto, K. J., Bell, R. E., Cochran, J. R., and Münchow, A.: Bathymetry in Petermann fjord from Operation IceBridge aerogravity, Earth and Planetary Science Letters, 422, 58–66, 2015.

Wang, M. and Overland, J. E.: A sea ice free summer Arctic within 30 years: An update from CMIP5 models, Geophysical Research Letters, 39, 2012.

Washam, P., Münchow, A., and Nicholls, K. W.: A decade of ocean changes impacting the ice shelf of Petermann Gletscher, Greenland, Journal of Physical Oceanography, 48, 2477–2493, 2018.

Washam, P., Nicholls, K. W., Münchow, A., and Padman, L.: Tidal modulation of buoyant flow and basal melt beneath Petermann Gletscher Ice Shelf, Greenland, Journal of Geophysical Research: Oceans, 125, e2020JC016 427, 2020.

Wilson, N., Straneo, F., and Heimbach, P.: Satellite-derived submarine melt rates and mass balance (2011–2015) for Greenland's largest remaining ice tongues, The Cryosphere, 11, 2773–2782, 2017.

Wood, M., Rignot, E., Fenty, I., An, L., Bjørk, A., van den Broeke, M., Cai, C., Kane, E., Menemenlis, D., Millan, R., et al.: Ocean forcing drives glacier retreat in Greenland, Science advances, 7, eaba7282, 2021.

Zhou, Q. and Hattermann, T.: Modeling ice shelf cavities in the unstructured-grid, Finite Volume Community Ocean Model: Implementation and effects of resolving small-scale topography, Ocean Modelling, 146, 101 536, 2020.